higher, controlled temperatures to force the solutes into the gas phase. Each of these gas-phase methods have been modified for use with the SPME approach to solute trapping.

Future Directions

Chemical extractions are thought to be a mature science. However, progress is still being made. The key influences driving these advances include the need for faster and more selective extractions and extractions that use smaller (if any) amounts of organic solvents. Better predictive models to aid the design and scale-up of extraction processes will also continue to be of great interest.

Further Reading

Barton AFM (ed.) (1990) *Handbook of Polymer–Liquid Interaction Parameters and Solubility Parameters*. Boca Raton: CRC Press.

Dean JR (1990) *Extraction Methods for Environmental Analysis*. New York: John Wiley & Sons.

Giddings JC (1991) *Unified Separation Science*. New York: John Wiley & Sons.

Handley AJ (ed.) (1999) *Extraction Methods in Organic Analysis*. Sheffield: Sheffield Academic Press.

Karger BL, Snyder LR and Horvath C (1973) *An Introduction to Separation Science*. New York: John Wiley & Sons.

Lide DR (ed.) (1994) *Handbook of Organic Solvents*. Boca Raton: CRC Press.

Morrison GH and Freiser H (1957) *Solvent Extraction in Analytical Chemistry*. New York: John Wiley & Sons.

Perry RH and Green DW (eds) (1997) *Perry's Chemical Engineer's Handbook*, 7th edn. New York: McGraw-Hill.

Rydberg J, Musikas C and Choppin GR (eds) (1992) *Principles and Practice of Solvent Extraction*. New York: Marcel-Dekker.

Wolf FJ (1969) *Separation Methods in Organic Chemistry and Biochemistry*. New York: Academic Press.

FLOTATION

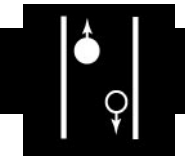

E. Woodburn, UMIST, Manchester, UK

Introduction

Overview of the Essential Elements of Separations Based on Froth Flotation

The objective of a flotation separation operation is to remove small hydrophobic particles from an aqueous suspension (pulp) by causing them to collide with, and to attach to, air bubbles. The bubble–particle aggregates rise through the suspension forming a froth at the upper surface of the pulp. The froth, which consists of the bubble–particle aggregates with inter-bubble water containing both hydrophobic and hydrophilic particles, forms a second phase where further enhancement of the hydrophobic/hydrophilic particle separation occurs, by water draining back to the pulp. The final product in which the hydrophobic particles are concentrated is removed as a froth overflow.

The science of the separation is primarily concerned with improving the selectivity of the hydrophobic particle attachment in the pulp through the addition of surface active chemicals. In addition, the hydrodynamics of the bubble–particle collision in the aerated suspension is important, as is the regulation of the drainage of water-containing hydrophilic particles from the froth by controlling its structure, also with surfactants.

It is probably fair to say that the industrial practice of flotation is effective even in the absence of a complete understanding of its scientific basis. The successful application of flotation separations in industry can be classified into three areas.

Mineral Processing

Froth flotation is a widely used technique in the mineral processing industry as an early step in the process of concentrating a valuable material from an ore. It is preceded by crushing and grinding and may be followed by leaching/(ion exchange) electrowinning or smelting. In data cited by Merrill and Pennington from a US Bureau of Mines survey for 1960 nearly 200 million tons of raw material were processed annually by flotation in the USA from which 20 million tons of concentrates were recovered. These consisted of 34 different commodities which, although principally metallic and non-metallic ores and coal, also currently reflects an increasing interest in recycling waste material.

More recent data supplied by Bowes, courtesy of the Anglo-American Research Laboratories in Crown Mines South Africa, is given in **Table 1**. These figures are estimates and should be used with caution, as the

Table 1 World-wide flotation tonnages (millions of tons), 1991–7

	1991	*1992*	*1993*	*1994*	*1995*	*1996*	*1997*
Copper	950	960	960	960	1000	1000	1080
Lead	93.3	91.4	79.2	78.4	78.4	84.3	87.5
Zinc	119.8	121.5	111.9	110.6	114.2	118.9	119.8
Nickel and cobalt	19.6	19.4	18.9	19.9	23.9	25.6	27.2
Iron	125	126	124	123	129	136	139
Phosphate	378	382	374	371	389	412	420
Industrial minerals	52	52	51	51	53	56	57
Coal	54	54	53	53	55	59	60
Totals	1791.7	1808.3	1772.0	1766.9	1842.5	1951.8	1990.5

Calculated based on the tonnages of pure metal produced; the mine production of ores are based on the following data:
Copper: average grade 0.8% Cu mined, at a processing recovery of 90%
Lead: average grade 3.0% Pb mined, at a processing recovery of 95%
Zinc: average grade 5.7% Zn mined, at a processing recovery of 82%
Nickel: average grade 1.6% Ni mined, at a processing recovery of 85%.
Source: Bowes (1997) Personal communication, Anglo-American Research Laboratories, Crown Mines, South Africa.

processing recovery refers to the flotation operation only. Where other recovery techniques are used such as leaching of nickel laterites and the recovery by leaching and solvent extraction of by-product cobalt from copper mining, these figures have not been included. Lead and zinc are often mined together and the separate tonnages reported for flotation processing may be overstated. The figures given for iron, phosphate, industrial minerals and coal are based on the percentages of the total tonnages. It is felt that particularly for iron and phosphate the figures may be excessive.

Overall the total ores processed annually using froth flotation given in Table 1 are consistent with the figure of 2 billion tons given by Fuerstenau in 1996. It is expected that significant growth will be seen in the next decade with flotation processing of copper ores rising to 1.6 billion tons per annum which represents 55% of the total tonnage anticipated.

Froth flotation has proved itself to be an important process in the mineral industry and will only become more important in the future.

Non-mineral Processing Recycling

This includes deinking wastepaper, separating individual components from plastic wastes, and effluent treatment of textile and smelter wastes.

Wastepaper deinking The growth of production has increased rapidly in recent years from 5.9 million tons per year in 1981 to 17.6 million tons per year in 1991. It is estimated that by 2001 the production of deinked waste will have increased to 31 million tons/year.

The objective of wastepaper deinking is to rid the grey repulped waste stock of unwanted particulates, usually inks. The reflectance of sheets of paper produced from the retreated waste pulp to light at 457 nm gives a measure of the brightness. However, changes in brightness are themselves not necessarily a complete description of the effectiveness of the separation of ink, as brightness changes are also associated with the presence of white inorganic fillers.

Prior to flotation the wastepaper is repulped in water at about a 15% suspension of fibre in water, in the presence of either a sodium soap or an anionic surfactant such as sodium dodecyl sulfate (SDS). These provide detergency, liberating the ink particles from their associated fibres. In some deinking plants this pulp is diluted to about a 1% fibre suspension, before being fed to a flotation separator in which the grey pulp suspension is aerated using cell designs similar to those in the mineral industry. The product stream from these cells is an inky foam, which is the reject, and a non-floated fibre suspension below the froth level which is the deinked product.

Although this process has some resemblance to minerals flotation there are significant differences. Specifically these relate to the properties of the fibre suspension. Their settling rate is low in any event, but as flocculated agglomerates they can trap small bubbles which give them a buoyancy that makes them easily entrainable in the water associated with the air bubbles forming the foam. This can result in the reject stream being as much as 10% of the feed, although the ink and its associated print vehicle oil will only account for between 1 and 2% of the feed fibre. Of this 1–2% only 10–20% is cellulose the rest being the oil/vehicle required for printing.

The mass of the reject stream is a serious environmental problem with land-fill costs rising sharply. There is also little information relating to the brightness increase of the deinked pulp as the removal of talc filler with the reject stream will seriously reduce the brightness of the final paper. It is clear that while deinking by flotation is potentially a valuable technique much fundamental work needs to be done before it reaches an acceptable level of separation.

Separation of plastic components from solid waste It has been said that of the 16.2 million tons of plastic waste generated annually in the USA only 2.4% is recycled with the rest being discarded to land-fill. As

mentioned earlier, this is becoming an increasingly expensive option and a scheme is envisaged where the individual components, polyethylene terephthalate (PET), polyethylene (PE), polyvinyl chloride (PVC) and polypropylene (PP), can be separated and hence become reusable.

PVC and PET can be separated from the others by gravity separation and by using 190 ppm of a surfactant, methyl iso-butyl carbinol (MIBC), at pH 11 in a 1% suspension of the solids, the PVC can be removed in a flotation froth giving high recoveries and purities, leaving pure PET in the unfloated tailings. This process, although at an early stage, offers a promising recycling opportunity.

Recovery of metals from refinery effluents It is possible that these may also respond to the use of froth flotation in transforming environmentally hazardous discharges into economically attractive sources of raw materials.

It is clear that considerable development work will be required in all the new applications and while it is sensible to make use of the extensive knowledge of the minerals industry of this separation technique, solving the special problems associated with each new application will most profitably be done by application of scientific fundamentals.

Water and Waste Treatment

Removal of contaminants from domestic water The technique of dissolved air flotation (DAF) is used as an alternative to sedimentation after flocculation in the preparation of water for domestic consumption. The bubbles are generated by first saturating a fraction of the treated raw water with air under pressure and then depressurizing in the total water. After depressurization the bubbles rise through the bulk solution, where they will be entrapped by the flocculated impurities. The bubble-floc aggregates rise to an overflow where they are removed. DAF differs from mineral flotation in that the bubbles are very small and are not stabilized by added surfactants, and there is no selective attachment. The justification for its use is that the aerated flocs rise faster than the settling rate of ordinary flocs whose density is close to that of water and whose structure favours a high resistance to settling flow.

Separation of dispersed oil from production water The processing of oil from offshore wells involves the removal of suspended solids from the oil and the separation of an oil–water mixture. Both the solid particles and the dispersed oil droplets are very fine; in the region of 10–50 μm. The processing involves the concentration of oil from a 5–50% by volume in water to 95–100% oil. This may involve a multistage operation particularly for very wet crudes, with a second concentrator stage treating the oil-rich product from the first stage to achieve the desired final oil purity.

If there is a second stage its water-rich waste stream is recycled to the first stage feed. The waste product from the first stage is water containing up to 0.1% oil by volume dispersed as ultrafine droplets. Before this water can be discharged, its oil content has to be reduced to comply with strict environmental standards both with respect to its oil content and the biological oxygen demand (BOD). Froth flotation has been used particularly in final clean-up units because of the small droplet size. DAF has been used as the bubbles coming out of solution following a reduction in pressure are thought to nucleate directly on the droplets. Unfortunately, the rise velocity of these air–droplet aggregates is so slow that extremely large cells are required. Their operation is in turn adversely affected by the pitching motions of floating rigs. Induced gas flotation (IGF) has also been used when the air is added to the feed stream at the throat of a Venturi nozzle. These have higher recovery rates but lower oil removal efficiencies than the DAF units. These reasons, together with the perceived high chemical costs, have favoured the use of liquid–liquid hydrocyclones in these situations.

Quantitative Measure of Flotation Performance

The performance of any separation unit is usually defined in terms of the fractional recovery (removal) R of the valuable product (contaminant) and its purity (concentration) in the product (waste) stream G.

Grade–Recovery Curves for Mineral Beneficiation

To characterize the flotation step in the beneficiation of a mineral ore, it is necessary to postulate that the mixture consists of at least two distinct particle populations, one largely valuable and the other principally waste (gangue). The gangue will invariably consist of several different mineral types, the presence of each being undesirable in the valuable mineral. Each population is characterized by a size distribution, and the amount of undesired material it contains. The fraction of misplaced material in a particular population can almost invariably be reduced by a sequence of size reducing steps usually consisting of primary and secondary crushing followed by fine grinding.

Increasing the fineness of grinding is said to liberate the valuable species from its associated waste

component. This will result in increasing the fraction of the desired component in the valuable mineral recovered and reducing its amount in the gangue. While liberation of the valuable component is clearly desirable, overgrinding will increase the power consumption of the mills, and as observed by Klimpel, also possibly introducing difficulties into the flotation process and subsequent downstream processing.

It is important to have a measure of the effectiveness of separation before an optimal solution can be identified. From a systems viewpoint, the flotation operation in mineral processing will separate a feed stream, F, into two product streams, a concentrate stream, C, containing an increased fraction of the valuable component and a tailings stream, T, containing a reduced amount of the valuable component. The following overall mass balance will apply:

$$Fx_F = Cx_C + Tx_T \quad [1]$$

where x_F, x_C and x_T are the mass fractions of the valuable component in the feed, concentrate and tailings, respectively. The performance measurement is characterized by two parameters. The fractional recovery R of the valuable component in the concentrate:

$$R = \frac{Cx_C}{Fx_F} \quad [2]$$

and its purity (grade) in the concentrate stream. The grade may simply be the mass fraction x_C or can be normalized between 0 and 1:

$$G = 1 - \frac{1 - x_C}{1 - x_F} \quad [3]$$

The upper limit, $G = 1$, clearly follows from the concentrate mass fraction of valuables, $x_C = 1$, while the lower limit, $G = 0$, presumes that the worst system performance is associated with no upgrading of the valuable mass fraction in the concentrate with respect to its concentration in the feed, although negative grades are mathematically possible.

Attainable Regions

The grade–recovery curve divides the grade–recovery space, $0 \leqslant G$, $R \leqslant 1.0$, into attainable and non-attainable regions. The grade–recovery curve is a function of a set of operational controls of which the fineness of grind of the feed is one. The others are actions that affect the selective attachment of the valuable component to air bubbles and the preferential drainage of the waste material back from the froth. The optimal performance of the flotation operation is defined in terms of the minimum cost of achieving a particular grade–recovery target.

Pulp Microprocesses

Wetting of the Particles' Surfaces

The particles are always dispersed in water and the nature of the wetting of their surfaces is critical for the effectiveness of the flotation separation.

Figure 1 shows the concept of an attached water film in which water dipoles are held by van der Waals forces together with ions held by electrostatic interaction with charges on the particle surfaces.

The stability of the adsorbed water film on the solid surfaces is clearly fundamental to the selective attachment of bubbles. Qualitatively for hydrophilic particles the water film is strongly bound to the solid, and hence is stable; conversely for hydrophobic solids the water film is weakly bound and will fail more readily.

The attachment of hydrophobic particles to bubbles is usually considered to consist of two sequential stages. First, the particle must collide with (intercept) the bubble. The second stage after interception has two components: (a) a bubble–particle contact time and (b) an induction time which is that required for the water film between the particle and bubble to thin to a point of failure at which point attachment is presumed to occur.

The selectivity of the separation is commonly enhanced by the adsorption of surface active chemicals onto the surfaces of the solid particles. These reagents have a molecular structure which has a polar and

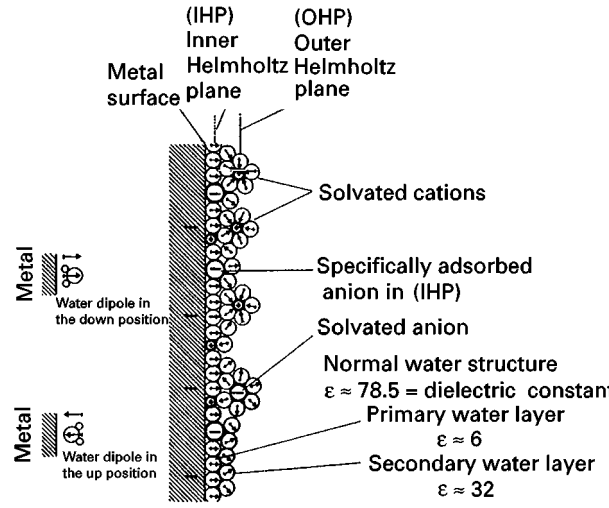

Figure 1 Model of a metal electrolyte interface showing film of water dipoles. Reproduced with permission from Leja J (1982) *Surface Chemistry of Froth Flotation*. New York: Plenum Press.

a non-polar end. Ideally, they will strongly attach to the valuable particles through their polar ends, with their non-polar ends confer an increased hydrophobicity. For the waste particles no attachment is considered to take place and consequently no hydrophobic increase will occur.

Clearly the choice of a suitable reagent is critical and is highly specific to a particular separation. Although the choice of reagent(s) for a particular separation usually has evolved with experience, the search for ever more effective reagent mixtures is an area of continuing research and development. A sound basis for these investigations is to develop an understanding of the free energy changes at the solid–water and bubble–water interfaces, consequent on changes of the reagent types and conditioning procedures.

Particle Surface Hydrophobicity

Theoretical basis for estimation To describe bubble–particle attachment after interception mathematically it is necessary briefly to review the nature and magnitude of the forces acting across the various interfaces.

After the initial interception, the particle and bubble will be separated by a water film. The film will become thin because of the forces of attraction between particle and bubble. The rate of thinning is determined by the dissipation of the kinetic energy of the particle on impact, associated with a resultant of long-range London–van der Waals molecular attraction (dispersion forces), capillary forces generated by the distortion of the bubble surface during the impact, electrostatic interactions between the uncompensated surface charges on the solid and those in the adjacent water layer, and as has been shown by Xu and Yoon, an additional force of attraction which appears to exist between two hydrophobic surfaces.

If the film thins to a critical value, failure will occur that will result in a successful attachment event. Both the thinning process and the critical thickness of the film must clearly depend on the interaction energy of the particle–water interface.

For the van der Waals forces of attraction, a treatment of the dispersion energy between a single gaseous atom and a slab of infinite extent is outlined by Adamson as:

$$\varepsilon(h_x)|_{\text{atom–slab}} = -\frac{\frac{\pi}{6} n C_1}{h_x^3} \qquad [4]$$

where $C_1 = \frac{3}{4} h \nu_0 \alpha^2$ and $\varepsilon(h_x)|_{\text{atom–slab}}$ is the potential energy of interaction in ergs/molecule at a separation distance h_x (cm), N_0 is the Avogadro number (6.02×10^{23} molecules/g mol wt) for water from Adamson, $h\nu_0 = 18$ eV ($= 18 \times 10^{-12}$ ergs), α (polarizability) $= 1.46 \times 10^{-24}$ cm^3. Since ρ_w density of liquid water g cm^{-3} and $n = N_0 \rho_w / 18 = 3.34 \times 10^{22}$ molecules/cm^3 using these figures $C_1 = 28.8 \times 10^{-60}$ ergs cm^6.

The dispersion energy between two infinite flat surfaces after integration is:

$$\varepsilon(h_x)|_{\text{slab–slab}} = -\left(\frac{\pi}{12}\right)\frac{(n^2 C_1)}{h_x^2} \qquad [5]$$

where $\varepsilon(h_x)|_{\text{slab–slab}}$ is in ergs cm^{-2}.

Fowkes has equated $\varepsilon(h_x)$ of eqn [5] to γ_s^d, the dispersion component of the total energy for water. As will be shown later, he has linked this dispersion energy with the physical adhesion energy at the interface between two different phases.

The dispersion energy for liquid water, γ_w^d, is calculated from eqn [5] to be 35.8 ergs cm^{-2} using the values given above and a value of 2.76 Å for the average intermolecular distance. This is somewhat higher than the experimentally determined value of 21.8 ergs cm^{-2} from contact angle measurements, but nevertheless it is valuable as it gives a theoretical basis for the forces of attraction at the interface between two immiscible phase surfaces. This is relevant to studies where the adsorption of a surfactant (collector) on a solid surface is used to modify the surface's hydrophobicity.

Eqn [5] is usually written in terms of, A, the Hamaker constant, which is specific for a given separation; for water $A = \pi^2 n^2 C_1 = 0.3 \times 10^{-12}$, and on average is of the order of 10^{-12} ergs:

$$\varepsilon(h_x)|_{\text{slab–slab}} = -\left(\frac{1}{12\pi}\right)\frac{A}{h_x^2} \qquad [6]$$

The attraction stress between the two surfaces is:

$$\frac{\partial \varepsilon(h_x)|_{\text{slab–slab}}}{\partial h_x} = \frac{A}{6\pi h_x^3} \text{ (dynes cm}^{-2}\text{)}$$

For a condensed system involving different phases the potential energy of interaction is still given by eqn [6] but with a modified Hamaker constant.

Consider a particle, 1, and an adjacent bubble, 2, in a water medium, 3. The particle and the bubble surfaces will be associated with water molecules. In the simplest case the film on the particle will consist of OH^- ions as well as molecular water dipoles and will be of the order of a monolayer in thickness,

which is the effective range of the van der Waals attractive forces. The bubble will have a layer of surfactant on its surface which will be orientated with its polar end in the water and the hydrophobic end in the air.

The interaction energy is expressed in terms of a net Hamaker constant, A_{132}, which is approximated by Adamson as a simple linear relationship:

$$A_{132} = A_{12} - (A_{13} + A_{23} - A_{33}) \qquad [7]$$

The binary Hamaker constants expressed above refer to two-surface interactions only. Some of these are physically difficult to interpret, but are nevertheless useful in formulating a conceptual understanding. With these reservations, A_{12} is the interfacial energy between a solid particle and a bubble separated by a vacuum and A_{33} is the interaction energy between water molecules.

A_{13} and A_{23} are the Hamaker constants representing the particle–water and bubble–water interaction energies. If these energies are low with respect to the mutual interaction energy of the water molecules then A_{132} will be greater than the interaction A_{12}. The enhanced attraction between the particle and the air bubble in the presence of water reflects *hydrophobic bonding*.

Leja quotes interaction energy potentials and London dispersion forces for various configurations following integration of atom–atom interaction energies. The dispersion force of attraction between two spheres of radius R_1 and R_2, for example, is given by:

$$\text{at } h_x \ll R_1, R_2, \qquad F = \frac{AR_1R_2}{6h_x^2(R_1 + R_2)} \qquad [8]$$

Experimental characterization of hydrophobicity – contact angle Interfacial energies for liquids may be measured by surface tension, while those for solid–liquid interfaces may be inferred from contact angle measurements.

If a liquid is placed on a solid surface it will form a droplet (**Figure 2**). The droplet will have a definite angle of contact, θ, with the surface. The change in the free energy ΔG^0 of the three-phase contact surface if the area of contact, ΔA_S, between the droplet and the surface were to change slightly is:

$$\Delta G^0 = \Delta A_S[(\gamma_{SL} - \gamma^0_{SV}) + \gamma_{LV}\cos(\theta - \Delta\theta)] \qquad [9]$$

where γ_{SL}, γ_{LV} and γ^0_{SV} are the interfacial energies for solid–liquid, liquid–vapour and solid–saturated vapour. At equilibrium this leads to the Young equation:

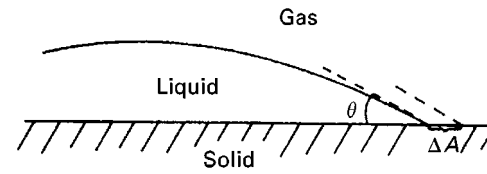

Figure 2 Contact angle θ of liquid droplet on a solid surface.

$$\lim\frac{\Delta G^0}{\Delta A_S} = 0, \quad \gamma_{SL} - \gamma^0_{SV} + \gamma_{LV}\cos\theta = 0 \qquad [10]$$

Bangham and Razouk observed that as γ^0_{SV} represented the energy of a surface in contact with a saturated vapour of partial pressure p^0, there must be present on the surface a film of condensed vapour with its own surface energy π^0. The total surface energy of the solid is thus:

$$\gamma_S = \gamma^0_{SV} + \pi^0 \qquad [11]$$

Substituting for γ^0_{SV} in eqn [10] gives:

$$\gamma_{LV}\cos\theta = \gamma_S - \gamma_{SL} - \pi^0 \qquad [12]$$

The interfacial energy of the solid–liquid interface γ_{SL}, can also be expressed as the sum of the surface energies of the individual phases separately, where γ_S is the surface energy of the solid, and γ_{LV} is the surface energy of the liquid in contact with vapour, and w_{SLV} is the work of adhesion which has to be subtracted:

$$\gamma_{SL} = \gamma_S + \gamma_{LV} - w_{SLV} \qquad [13]$$

The work of adhesion for the three-phase contact is then obtained from the Young equation after substituting for γ_{SL} from eqn [12] into eqn [13]:

$$w_{SLV} = \gamma_{LV}(1 + \cos\theta) + \pi^0 \qquad [14]$$

Equation [14] is a form of the Dupré equation that relates an increasing contact angle to a reduction in the adhesion energy between the solid surface and water, or alternatively to an increase in the hydrophobicity of the solid surface.

Fowkes modified the Girifalco-Good equation for the work of adhesion and suggested that it was due to the London–van der Waals dispersive forces in each phase rather than the total intermolecular energies. Equation [15] describes the resulting expression for the interface energy between a solid

and liquid:

$$\gamma_{SL} = \gamma_S + \gamma_{LV} - 2\Phi\sqrt{(\gamma_S^d \gamma_L^d)} \qquad [15]$$

(Φ is commonly taken as unity).

Fowkes applied eqn [15] to eqn [12], to express a relationship between the contact angle and the dispersive energy of the solid surface, γ_S^d, this being considered to be a parameter most characteristic of the influence of the nature of the surface on the interface phenomena important in flotation:

$$\begin{aligned} \gamma_{LV}\cos\theta &= -\gamma_{LV} + 2\sqrt{(\gamma_S^d \gamma_L^d)} - \pi^0 \\ \cos\theta &= -1 + 2\sqrt{\gamma_S^d}\left[\frac{\sqrt{\gamma_L^d}}{\gamma_{LV}}\right] - \frac{\pi^0}{\gamma_{LV}} \end{aligned} \qquad [16]$$

The dispersion forces in a particular solid, γ_S^d, can therefore be estimated by using contact angle measurements with different liquids obviously of known surface dispersion γ_L^d. Linear plots of $\cos\theta$ against the ratio of dispersive energies of the liquids confirm the validity of eqn [16] and the slope of the line gives $\sqrt{\gamma_S^d}$.

Experimental characterization of interfacial energies – adsorption studies Adsorption data may be used to estimate π which reflects changes in interfacial energies. These require knowledge of the adsorption isotherm, relating Γ, the mols of vapour adsorbed per square centimetre of solid surface with p, the partial pressure of the solute in the gas.

Bangham and Razouk derived an expression for π by integrating the Gibbs equation. This states that:

$$\mathrm{d}\gamma = -\Gamma RT \mathrm{d}\ln p$$

from which:

$$\begin{aligned} \pi &= -\int \mathrm{d}\gamma = RT\int \Gamma \mathrm{d}\ln p \\ \pi &= \gamma_S - \gamma_{SV} = RT\int_0^p \Gamma \mathrm{d}\ln p \\ \pi^0 &= \gamma_S - \gamma_{SV}^0 = RT\int_0^{p^o} \Gamma \mathrm{d}\ln p \end{aligned} \qquad [17]$$

Harkins by defining γ_{SV} as being equal to $\gamma_{SL} + \gamma_{LV}$ related the energy π of the adsorbed liquid film to the surface activities:

$$\pi = \gamma_S - (\gamma_{LV} + \gamma_{SL}) \qquad [18]$$

By substituting for γ_{SL} from eqn [15], Fowkes obtained an expression which links γ_S^d with π as determined from adsorption studies:

$$\pi = 2\sqrt{(\gamma_S^d \gamma_L^d)} - 2\gamma_{LV} \qquad [19]$$

The derivation assumes that the adsorption of vapour is determined solely by dispersion forces (physical adsorption):

$$\gamma_S^d = \frac{(\pi + 2\gamma_{LV})^2}{4\gamma_L^d} \qquad [20]$$

It is clearly of interest to compare the surface free energies γ_S^d determined from gaseous adsorption studies with those obtained from contact angle measurements. Fowkes quotes an average value of 122 ergs cm^{-2} for the dispersive energy of a graphite surface, γ_S^d, from the adsorption of N_2 and n-heptane, which compares well with the value of 109 ergs cm^{-2} from contact angle measurements of a water droplet on a graphite surface ($\theta = 85.7^\circ$ and $\pi^0 = 19$ ergs cm^{-2}).

The surface free energies can also be experimentally determined from heats of immersion ΔH_i since:

$$\begin{aligned} \gamma_{SL} - \gamma_S &= \gamma_{LV} - 2\sqrt{(\gamma_S^d \gamma_L^d)} \\ \Delta H_i &= (\gamma_{SL} - \gamma_S) - T\left(\frac{\mathrm{d}\gamma_{SL}}{\mathrm{d}T}\right) \\ \Delta H_i &= \gamma_{LV} - 2\sqrt{\gamma_S^d \gamma_L^d} \\ &\quad - T\left[\frac{\mathrm{d}\gamma_{LV}}{\mathrm{d}T} - 2\sqrt{\gamma_{LV}^d}\frac{\mathrm{d}\sqrt{\gamma_S^d}}{\mathrm{d}T} - 2\sqrt{\gamma_S^d}\frac{\mathrm{d}\sqrt{\gamma_{LV}^d}}{\mathrm{d}T}\right] \end{aligned} \qquad [21]$$

Experimental characterization of interfacial energies – heat of immersion Equation [21] can be used with heats of immersion measured calorimetrically to determine the contribution of polar interactions between the solid and the liquid into which it has been immersed. If dispersion forces only were significant at the interface, then the equality of eqn [19] should hold. Deviations from the equality of eqn [19] referred to as the excess by Fowkes are a measure of the strength of the polar interaction:

$$\text{the excess} = (\pi + \gamma_{LV}) - 2\Phi\sqrt{(\gamma_S^d \gamma_L^d)} \qquad [22]$$

Table 2 Polar interfacial interactions at solid–liquid interfaces

Solid	*Liquid*	$2\sqrt{(\gamma_S^d, \gamma_L^d)}$ *(ergs cm^{-2})*	$\pi + 2\gamma_{LV}$ *(ergs cm^{-2})*	*Excess (ergs cm^{-2})*
Graphite	n-Heptane	96	96	0
	Benzene	114	134	20
Silica	n-Heptane	100	100	0
	Benzene	118	138	20
	Acetone	98	156	58
	n-Propanol	98	182	84
	Water	94	462	368

Reproduced with permission from Fowkes FM (1964) The Interface Symposium. *Industrial and Engineering Chemistry* 56(12), 40–52, Table IX.

Table 2 shows polar interactions at some solid–liquid interfaces in terms of the excess.

From the limited data reproduced in table it can be seen that the adsorption of hydrocarbons both on graphite and silica is principally through dispersion forces while that of n-propanol and water on silica show significant polar interactive forces. Clearly, the presence of these strong attractive forces will result in very stable films.

The Forces Between a Charged Particle Surface and an Ionic Solution

Origin of particle surface charge The attraction between a charged surface and a concentration of counterions in the diffuse double layer adjacent to the particle surface will be the source of increased interaction energies. The charge density on the surface of the solid particles, and hence the potential gradients in the diffuse double layers, is determined by the degree to which the intermolecular forces at the crystal surface are non-compensated. These are related to the structure of the crystal lattice and to the orientation of the cleavage planes at the surface.

As a consequence of a surface charge, to a greater or lesser extent hydrated ions will be adsorbed, the energy of attachment being related to the charge density on the particle surface. As both orthorhombic sulfur and graphite exhibit comparatively weak residual surface forces with strong non-polar bonds being localized within the unit cells of the crystal lattice, the attachment energy of hydroxyl and hydrated ions will be low giving the surfaces their hydrophobic character.

On the other hand, for ionic crystals the uncompensated electrostatic forces at the surface may be high and can lead to strong attachment of water. As the electrostatic forces operate over significantly longer distances than do the London–van der Waals forces they will give hydrated layer thicknesses of the order 20–60 Å. According to Klassen and Mokrousov who quote Derjaguin and Derjaguin, Karasiev and Zorin, the hydrated layer has an increased viscosity over that of the bulk water and the change in viscosity is discontinuous.

Diffuse boundary layer To illustrate the previous observations consider a plane surface with a uniform charge density σ_0 in contact with water with a bulk ionic concentration n_0. If the solid–water interface has a positive electrical potential, ψ_0, the potential in the solution will decrease to 0 as one proceeds in a normal direction away from the surface into the solution. Close to the positively charged surface, however, there will be an excess of negative ions. If n^+ and n^- are the concentrations of the positive and negative ions, of equal and opposite charge, $+z$ and $-z$, respectively, at a point in the solution then the net charge density ρ at that point in the solution will be:

$$\rho = ze(n^+ - n^-) \qquad [23]$$

Using the Boltzmann factor, the ionic concentrations can be linked to the local potential at a point in the solution:

$$n^- = n_0 \exp\left(\frac{ze\psi}{kT}\right)$$

and:

$$n^+ = n_0 \exp -\left(\frac{ze\psi}{kT}\right)$$

from which:

$$\rho = -2n_0 ze \sinh\left(\frac{ze\psi}{kT}\right) \qquad [24]$$

The integral of ρ to infinity will give the total excess charge in the solution per unit cross-sectional area which is equal to but opposite in sign to the charge density on the surface σ. The situation is that of a double layer of charge, the one localized on the solid surface and the other in the diffuse region.

To link the potential in the solution with the normal distance x from the surface the Debye–Hückel treatment may be followed. This uses Poisson's equation which relates the divergence of the gradient of the electrical potential at a given point to the charge

density at that point:

$$\nabla^2\psi = -\frac{4\pi\rho}{D}$$

$$\nabla^2\psi = \frac{8\pi n_0 ze}{D}\sinh\left(\frac{ze\psi}{kT}\right) \qquad [25]$$

where ∇^2 is the Laplace operator and D is the dielectric constant of the medium (for water = 78). For small values of $ze\psi$ with respect to kT, eqn [25] can be expressed as:

$$\nabla^2\psi = \kappa^2\psi$$

$$\kappa^2 = \frac{8\pi n_0 z^2 e^2}{DkT} \qquad [26]$$

The treatment for a plane charged surface is due to Gouy and Chapman (after defining):

$$y = \frac{ze\psi}{kT} \quad \text{and} \quad y_0 = \frac{ze\psi_0}{kT} \qquad [27]$$

Eqn [26] can be written as:

$$\frac{d^2y}{d^2x} = \kappa^2 \sinh y$$

with the boundary conditions at:

$$x = \infty, y = 0 \quad \text{and} \quad \frac{dy}{dx} = 0 \qquad [28]$$

For the case where y_0 is small, for example for univalent ions at room temperature, $\psi_0 < 25$ mV, the solution of eqn [28] reduces to:

$$\psi = \psi_0 \exp -\kappa h_x \qquad [29]$$

setting $x = h_x$ as the separation distance.

The quantity $1/\kappa$ is the distance from the surface where the potential in the solution reaches $1/e$ ($= 0.3679$) of its value at the surface; the plane $1/\kappa$ is used to represent the thickness of the diffuse layer adjacent to the surface. The charge density of the solid surface can be obtained from a knowledge of $\psi(x)$ vs x since:

$$\sigma_0 = -\int_0^\infty \rho\, dx = \frac{D}{4\pi}\int_0^\infty \frac{d^2\psi}{dx}\, dx$$

$$= -\left(\frac{D}{4\pi}\right)\left(\frac{d\psi}{dx}\right)\Bigg|_{x=0} \qquad [30]$$

For small potentials, the diffuse double layer can be likened to an electrical condenser of charge density σ_0 and a plate separation of $1/\kappa$.

Figure 3 shows very interesting relations between $\psi(x)$ and x and between σ_0 and ψ. Figure 3(A) shows the exponential decay in the solution potential for a surface whose potential ψ_0 is 25 mV, while Figure 3(B) shows that increasing the concentration of the bulk solution of univalent ions, from 0.001 to 0.01 M significantly reduces the dispersion layer thickness from almost 200 to less than 40 Å.

Figure 3(C) shows a reduction of dispersion layer thickness of similar magnitude to that reported in Figure 3(B) following the replacement of a 0.001 M univalent solution by a 0.001 M divalent solution. Figure 3(D) and (E) show the relation between the

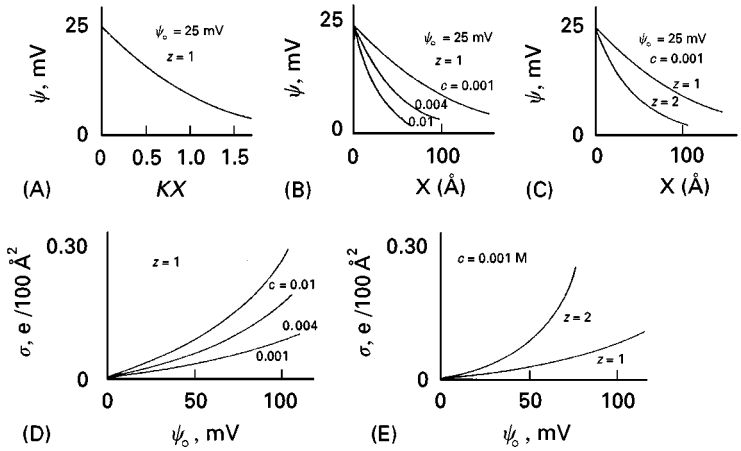

Figure 3 The diffuse double layer. Reproduced with permission from Adamson AW (1982) *Physical Chemistry of Surfaces*, 4th edn. New York: John Wiley.

surface charge density (e/100 Å^2) and the surface potential ψ_0.

Conversion to SI units requires a conversion constant, the permittivity (of vacuum), $\varepsilon^0 = 8.859 \times 10^{-12}$ coulombs/(metre volt). The conversion in cgs/esu to SI units of the potential ψ and the charge e is given in eqn [31]:

$$\psi_{\text{cgs/esu}} = \psi_{\text{SI}} \times (4\pi\varepsilon^0)^{1/2} \quad \text{and} \quad e_{\text{cgs/esu}} = \frac{e_{\text{SI}}}{(4\pi\varepsilon^0)^{1/2}} \qquad [31]$$

To illustrate the use of the conversion constant, the intercharge energies between two charged surfaces, as given by Coulomb's law, are:

$$\text{in CGS units} \quad \varepsilon(\text{ergs}) = \frac{q_1 q_2}{h_x D}$$
$$\text{in S.I. units} \quad \varepsilon(\text{Joules}) = \frac{q_1 q_2}{4\pi\varepsilon^0 h_x D} \qquad [32]$$

The equivalent equation in SI units to eqn [26] then becomes:

$$\nabla^2\psi = \frac{2n_0 z^2 e^2}{\varepsilon^0 DkT}\psi = \kappa^2\psi \qquad [33]$$

To illustrate the magnitude of κ, consider a 1 mM solution in water of a uni-univalent solute. In this case the number of molecules, n_0, of solute per cubic metre is just the Avogadro number, $N_0 = 6.02 \times 10^{23}$. Note also that $\varepsilon^0 D$, sometimes written only as D, is $= 6.91 \times 10^{-10}$ coulombs/(volt metre). Substituting parameters for this case in the relationship for κ implied in eqn [33], a value for κ of 1.0×10^8 m^{-1} is obtained, or $1/\kappa = 10$ nm.

The Stern treatment of the electrical double layer The Gouy–Chapman treatment gives absurd answers for small values of κh_x when ψ_0 is large. Adamson illustrates this point with the example for $\psi_0 = 300$ mV:

$$y_0 = \frac{300}{25.69} = 12 \qquad [34]$$

if $n_0 = 0.001$ M then $n^- = 0.001 \times e^{12} = 160$ moles/litre! This is due to the treatment of the charges as point sources by neglecting the ionic diameters.

Stern suggested that the region in the liquid adjacent to the surface be divided into two parts, an inner compact layer consisting of ions or hydrated molecules which are firmly attached to the surface, and an outer diffuse layer in which the ions were less firmly bound. The key to his analysis is the estimation of the extent to which solute molecules will enter the compact layer, which requires them to displace water dipoles, in particular.

If S_0 is the number of occupiable sites on the surface then the maximum charge density for the compact layer is $\sigma_0 = zeS_0$. In the presence of a dilute solute phase, however, the ratio of the sites occupied by the solute to those potentially occupiable is proportional to, N_S, the mole fraction of solute. In dilute solution, Stern linked this fraction and the potential ψ_δ at the outer surface of the compact layer to a charge density σ_S in the compact layer, with ϕ allowing for any additional chemical adsorption potential. This approximates to:

$$\frac{\sigma_S}{\sigma_0} = \frac{N_S \exp[-(ze\psi_\delta + \phi)/\kappa T]}{1 + N_S \exp[-(ze\psi_\delta + \phi)/\kappa T]} \qquad [35]$$

This suggests that the charge σ_S in the compact layer can be linked to the potential at its outer boundary ψ_δ, using eqn [30] with the approximation:

$$-\left.\frac{\mathrm{d}\psi}{\mathrm{d}x}\right|_0 \approx \frac{\psi_0 - \psi_\delta}{\delta} \quad \text{hence} \quad \sigma_S \approx \frac{D'}{4\pi\delta}(\psi_0 - \psi_\delta) \qquad [36]$$

where δ is its thickness and D' is an apparent dielectric constant for the layer.

In the diffuse layer as one proceeds outwards from the surface a potential at position x can be calculated using eqn [29] with ψ_δ replacing ψ_0. The ions are mobile in this layer and the layer is characterized by a thickness $= 1/\kappa$.

The electrodynamic potential (ζ) A charged surface experiences a force in an applied electric field. As it moves the boundary of the water moving with it is the shear plane of thickness $1/\kappa$, which has a potential $\psi(1/\kappa)$, commonly referred to as the zeta-potential (ζ).

The potential of the shear plane can be experimentally determined by electrophoresis. If for a spherical particle of radius R_p, the charge density of the diffuse layer up to the shear plane is σ_D, the force exerted on it in an electric field of F_S (V m^{-1}) will be:

$$f_E = \sigma_D \times F_S \times 4\pi R_p^2 \text{ (newtons)} \qquad [37]$$

this will cause it to move at a velocity at which the viscous drag is equal to the applied electrical force. From Stokes' law the shear resistance f_S, of a particle

of radius R_p, moving at a velocity v is given by:

$$f_S = 6\pi\mu R_p v \quad \text{which gives} \quad v = \frac{2\sigma_D F_S R_p}{3\mu} \quad [38]$$

The relation between the charge density, σ_D, of the diffuse layer and the potential at the shear plane treated as a parallel plate condenser with plates $1/\kappa$ apart in SI units is:

$$\sigma_D = \varepsilon^0 D\zeta\kappa \quad (\text{coulombs m}^{-2}) \quad [39]$$

If the ζ-potential of a spherical particle, of radius 1 μm moving in an external field of $1\,\text{V cm}^{-1}$ is 25 mV, then the velocity calculated from eqns [38] and [39] is $1.15 \times 10^{-6}\,\text{m s}^{-1}$. Data quoted by an equipment manufacturer gives a velocity $v = 2.0 \times 10^{-6}\,\text{m s}^{-1}$, for the same conditions.

The charge density σ_D of the diffuse layer follows from the ζ-potentials measurements. The charge density of the surface, σ_0, follows as the sum of the charge densities of the compact layer σ_S and σ_D.

Collectors

General A collector is a surface-active chemical which has a polar and a non-polar group. The work of adhesion of a collector to a solid surface has been separated into three components by Leja:

$$w_{SLV} = w^d + w^h + w^i \quad [40]$$

where w^d is the dispersive component, w^h is the energy associated with polar adsorption of water at non-ionic sites and w^i is the contribution through electrostatic interactions with the Stern layer associated with the solid surface (**Figure 4**).

The collector molecule must be firmly attached to the solid surface through its polar group and must be able to confer sufficient hydrophobicity to the surface through the non-polar component to facilitate bubble attachment. It appears that for effective attachment, multilayer adsorption is required. Fuerstenau and Fuerstenau have suggested that the multilayer arise from the dispersive interactions between the non-polar parts of the molecules; they have referred to the resulting structure of the adsorbed layer as hemimicelles.

The attachment of a bubble to the solid ultimately involves an interaction between the polar groups adsorbed on the bubble surface and the multilayered collector on the particle's surface. As the science of the interactions is still imperfectly understood it is necessary briefly to review the nature of the collector in specific separations.

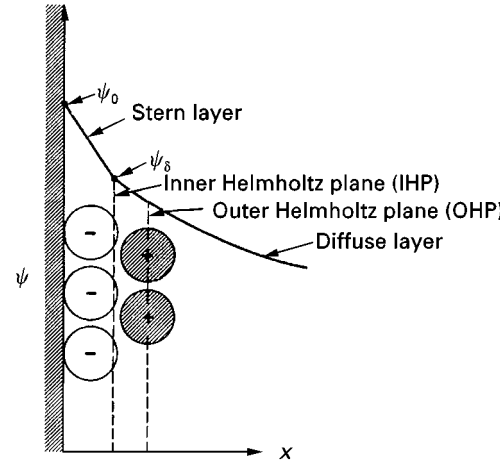

Figure 4 The Stern layer. Reproduced with permission from Adamson AW (1982) *Physical Chemistry of Surfaces*, 4th edn. New York: John Wiley.

Thiol collectors The discovery of xanthates in the 1920s caused a rapid increase in the flotation process generally, but specifically with nearly all the sulfide ores. While they confer hydrophobicity on sulfide minerals, they do not affect the flotation of silicates, aluminosilicates, oxides or mineral salts. However, to achieve selective separation between sulfides within the same ore-body careful choice of reagent and control of operating conditions is required.

Although there appears to be a wide range of these sulfur-bearing compounds, they are derived from a restricted number of oxygen-bearing compounds through the substitution of sulfur for the oxygen. The great majority are derived from carbonic, carbamic and phosphoric acids, urea and the alcohols. They are usually surface-active with respect to the liquid–solid interface, but less so at the bubble–liquid surface. Some of the most important of these sulfhydryl collectors are discussed below, with their structures given in **Figure 5**(A). In all cases R denotes a non-polar group.

Alkyl dithiocarbonates or xanthates ($R{-}O{-}CS_2^- M^+$) Potassium ethyl xanthate (KEtX) is used for the selective flotation of Cu–Zn, Pb–Zn and Cu–Pb–Zn sulfides. The effective recovery of the sulfide increases with the length of the alkyl group R; n- and iso-propyl and butyl giving increased recovery over the ethyl homologue but with a reduced selectivity. These conflicting trends increase up to amyl and hexyl. All the xanthates mentioned are soluble in water and are restricted to a pH range of 8–13 as they undergo hydrolysis under more acid conditions.

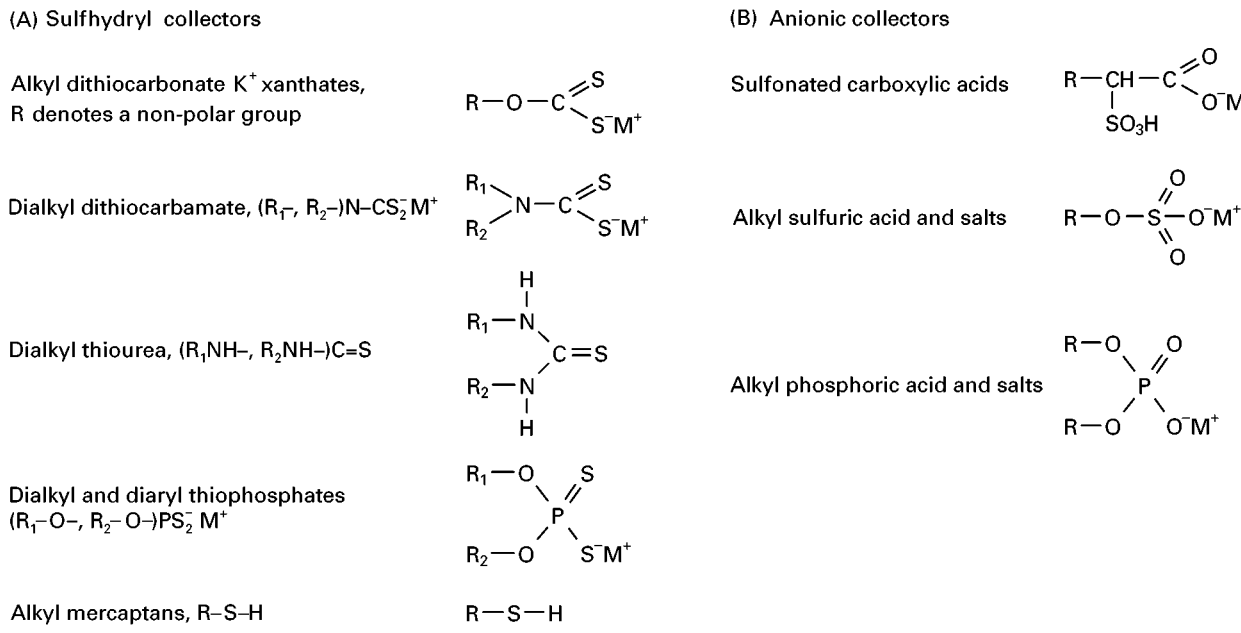

Figure 5 Industrial flotation reagents.

Dialkyl dithiocarbamate (R_1–, R_2–)N–$CS_2^- M^+$ These are selective collectors for Cu or Cu-activated Zn from FeS_2. They are sparingly soluble and are used as emulsions in the pH range 4–9. The non-polar group R_1 is usually CH_3 or C_2H_5 while R_2 is either propyl or butyl.

Dialkyl thiourea (R_1NH–, R_2NH–)C=S These are selective collectors for Cu, Pb and Ag ores and have been used in the flotation of complex Cu–Pb–Zn ores. They are not water soluble and have to be used as dispersions in water.

Dialkyl and diaryl thiophosphates (R_1–O–, R_2–O–)$PS_2^- M^+$ The di-ethyl and di-sec-butyl derivatives are used as collectors for Au, Ag and Cu. The dicresyl derivative is used for Ag, Cu, Pb and Zn. Generally, the dithiophosphates (DTP) reagents are more selective than the xanthates particularly in preventing the flotation of iron sulfides. The alkyl derivatives are water-soluble and are used in 5–20% solutions over the pH range 4–12. The most common alkyl homologues are diethyl and dibutyl. The alkyl derivatives are essentially non-frothing.

The aryl derivatives are dicresyl and exhibit frothing behaviour. They are not water soluble and are used undiluted.

Alkyl mercaptans R–S–H Only homologues higher than C_{12} have been used. Dodecyl mercaptan is a powerful non-selective collector particularly for Cu. The mercaptans are not water soluble and are used either in an organic solution or as a liquid emulsion.

Xanthate derivatives R–O–$S_2^- M^+$ These are used mainly in Cu flotation. They are water insoluble and are used either as an aqueous emulsion or as an organic solution. They are effective over a wide pH range.

Anionic collectors These are ionizable non-thio compounds derived from carbonic, sulfuric, phosphoric, phosphonic and arsonic acids (Figure 5(B)). They are anionic, depending on the pH of the flotation pulp and are used to collect a wide range of oxide, silicate and salt-type minerals. These minerals usually have positive ζ-potentials and consequently bind OH^- ions giving them a hydrophilic character. For the adsorbed surface to become hydrophobic the non-polar part of the anionic collector molecules must have longer carbon chains than those of the thiols. Their attachment is primarily through electrostatic interactions between the polar group of the collector and the particle surface while dispersive interactions between the non-polar groups of adjacent collector molecules increase the hydrophobicity of the surface by producing multilayered adsorbed films.

Fatty acid salts R–$COO^- M^+$ The cation M^+ is either Na^+ or K^+, with very few exceptions they operate at high pHs where they are highly dissociated.

The non-polar radical R most used lies in the C_{16}–C_{18} range, typically oleic, linoleic and linolenic.

Unsaturated molecules are preferred. At alkaline pH the metal salts are soluble in water. They are used for the flotation of apatite, calcite, fluorspar and barite. Because of the electrostatic nature of their adsorption they are very powerful collectors for surfaces with positive ζ-potentials but selectivity is difficult to effect and requires careful control of the chemical environment which usually requires the use of depressants.

Alkyl sulfuric acid and salts $R–O–SO_3^-M^+$ These are stronger acids than the fatty acids and exist in an ionized water-soluble form above pH 1–2; the alkyl radical is usually C_{12} and saturated. Organic sulfates and sulfonates are used to float oxides and silicates such as iron ores, chromite, garnet, beryl and zircon. As the bonding with the solid surface is primarily electrostatic, pH control is critical, especially for the shorter chain length alkyl groups, as it affects their intermolecular dispersive bonding.

Alkyl and aryl sulfonic acid and salts $R–SO_3^-M^+$ A typical collector of this type is sodium dodecyl benzene sulfonate $C_{12}H_{25}–C_6H_4–SO_3–O^-Na^+$ which is a strong acid and will operate in pulps with pH values above 2.

Alkyl phosphoric acid and salts $(R_1O–, R_2O–)PO_2^-M^+$ R_1 and R_2 can be either aliphatic or aromatic. Dialkyls are more strongly frothing than the monoalkyls. They are used in separations from quartz gangue, in particular for the separation of heavy minerals from glass sands. They have also been used in flotation of tungsten, uranium and phosphate ores. They are not selective in the presence of apatite, calcite, fluorspar or barite.

Cationic collectors This group consist of amines which below ceratin pH values exist in the cationic form, RNH_2, R_1R_2NH, $R_1(R_2)_2N$. The amines are insoluble in the free base form but are treated by acids such as acetic or hydrochloric to solubilize them. They ionize in aqueous solutions as follows:

$$RNH_2(aq) + H_2O = RNH_3^+ + OH^-$$

Typical collectors of this type are a primary aliphatic amine, n-amylamine ($C_5H_{11}NH_2$), a primary aromatic amine, aniline ($C_6H_5NH_2$), and pyridine (NC_5H_5), nitrogen in a benzene-like nucleus.

Particularly important are the quaternary ammonium salts, $R_1(R_2)_3N^+X^-$, which ionize strongly and are water soluble. The collecting action of this group is based on being strongly attached to surfaces with negative ζ-potentials and are consequently rarely selective but are effective over a wide pH range. Important collectors of this type include alkyl propylenediamine, $(RNH_2(CH_3)_3NH_3)^{2+}2X^-$, and tetradecyltrimethylammonium bromide (TTAB), $CH_3(CH_2)_{13}–(CH_3)_3–N^+Br^-$.

Cationic collectors are used to separate sylvite (KCl) from halite (NaCl) in brine and are also used in the separation of silica from phosphate and in the flotation of zinc carbonates and silicates.

The Mechanism Associated with the Flotation of Some Important Ores

Sulfides – recovery of galena – effect of collectors Most data are associated with the flotation of the lead ore galena PbS, which has been studied extensively. Although the tonnage of lead ore processed is only a tenth of the amount of the copper ores processed (Table 1), the fact that it exists in only one valence state simplifies data interpretation. The overall mechanism for copper sulfide ore processing is accepted as being similar to that of lead despite the copper valence change under oxidizing conditions. Both copper and lead are floated with sulfhydryl collectors and it is of interest to review the concepts associated with the collector action. It is often the case that, despite the high selectivity of the sulfhydryl collectors for sulfides in the presence of oxide and silicate gangues, that further selectivity between different sulfide minerals is required. It is consequently not necessarily sufficient to determine optimum recovery for a specific collector, but it is also necessary to investigate its effect on the simultaneous recovery of an undesired sulfide mineral.

The effect of oxygen on the ζ-potential and KEtX adsorption on a galena surface In the absence of oxygen the adsorption density of ethyl xanthate is independent of pH and remains constant at a level of 2×10^{-6} g moles/g of galena, which corresponds to effectively a coverage of a monolayer assuming one xanthate ion adsorbed at one lead site on the surface. The area occupied by an anion of amyl xanthate disposed perpendicularly to the surface of a mineral is given by Klassen and Mokrousov to be 28 Å^2. This adsorption area should be independent of the length of the hydrocarbon chains of normal xanthates.

However, the adsorption density does fall as the length of the alkyl chain increases to about half the monolayer adsorption density with octyl xanthate. Additionally, in the absence of both oxygen and xanthate, the ζ-potential vs pH curve for galena, falls from $+20$ mV at pH 2 to -40 mV at pH 12. The pH at which the ζ-potential is zero is called the point of zero charge (PZC) which is a useful characterizing parameter.

In the presence of 1×10^{-3} molar ethyl xanthate the ζ-potential remains steady at -40 mV over the pH range of 4–12.

This seems to indicate that the attachment is due to the chemisorption of the alkyl part of the xanthate molecule on the galena surface, presumably after displacing H_3O^+ or OH^- ions. The unchanged outer negatively charged compact surface layer is associated with the polar end of the molecule.

In the presence of oxygen, but without xanthate, the ζ-potential vs pH differs significantly from the previous case. Over the pH range from 4 to 6 the ζ-potential vs pH curve is convex upwards with a maximum of just under $+20$ mV at pH 6. At increasing pHs the ζ-potential falls to 0 at pH 6.9, the PZC; from 6.9 to 12 it falls from 0 to -40 mV. It should be noted that for the previous case of no oxygen and no xanthate the pH at the PZC is 2.6.

In the presence of 1×10^{-4} mol L^- ethyl xanthate and oxygen, the ζ-potential–pH curve is again electronegative over the range 4–12, as with the case for xanthate without oxygen, but is no longer constant, falling from -20 mV at pH 4 to -40 mV at pH 12.

There are conflicting explanations for the effect of oxygen on the galena surface. One plausible theory is that, in the presence of oxygen, the surface is oxidized to thiosulfate and sulfate. As air also contains CO_2, lead carbonates may also form displacing the sulfates. Some of these surface compounds may move into the inner compact layer in the solution. In the presence of xanthates, a significant xanthate fraction may react directly at the surface, possibly with the sulfates, forming a strong bond with the lead mineral. The rest of the xanthate will displace the sulfate from the inner to the outer compact layer, causing the potential at the outer compact layer ψ_δ to remain electronegative.

It is further postulated that with excess xanthate, metathetic replacement of the sulfate will occur producing uncharged hydrophobic, insoluble lead ethyl xanthate. This process is clearly kinetic requiring diffusion of the unreacted sulfate at the surface through the compact layer. Multiple layers of the insoluble lead ethyl xanthate will confer increased flotability on the galena. Finkelstein, Allison, Lovell and Stewart reported improved flotation recoveries for galena using ethyl xanthate in terms of the thickness of the lead ethyl xanthate layers expressed as monolayers. The recovery increased from zero with no ethyl xanthate to 70% for a single monolayer increasing to 95% with five monolayers.

Selective flotation of galena – effect of depressants Reagents which, to a greater or lesser degree depress recoveries of sulfides (depressants), include OH^-, S^{2-} and chromate.

Fuerstenau in 1982 reported 100% recovery of galena, using 1×10^{-5} mol L^{-1} ethyl xanthate in the presence of oxygen, over the pH range 2–10. However, if the lead content (grade) of the concentrate is required to be low in the presence of other sulfides, which are themselves being floated by the 1×10^{-5} mol L^{-1} ethyl xanthate, this requires a reduction (depression) of the galena recovery simultaneously with a smaller reduction in the recovery of the desired sulfide.

Depression of galena using hydroxyl is effected at pH values greater than 11, due to the formation of $HPbO_2$, which is the unhydrated form of $Pb(OH)_3^-$, in the Stern compact layer, this causes the galena surface to become hydrophilic with consequent reduction in lead recovery.

The depression of galena using sodium sulfide is much greater than that of all other sulfide minerals. Additions of sodium sulfide to a galena suspension in xanthates will cause an insoluble hydrophilic lead sulfide rather than lead xanthate to form at the solid surface according to the reaction:

$$PbS(s) + 2EtX^- = Pb(EtX)_2(s) + S^{2-}$$

In the presence of chromate the adsorption of xanthates does not decrease, but when lead chromate forms on the surface, the hydration of the chromate is so strong that the collector hydrophobicity is significantly reduced.

Grade-recovery of copper ores In view of the economic importance of chalcocite (Cu_2S) and chalcopyrite ($CuFeS_2$) their selective recovery from ores containing undesired pyrites will be briefly reviewed.

Depression of pyrite – Effect of pH. Flotation of pyrite will be possible with short-chain xanthates such as potassium ethyl xanthate at pHs below 11. At addition rates of 2×10^{-4} mol L^{-1} of KEtX, 100% recovery is possible. The recovery is thought to be due to the adsorption of dixanthogen on the surface. However, at high pH values xanthate oxidation to dixanthogen does not occur according to the reaction shown below, thus depressing the pyrite recovery:

$$2X^- + \tfrac{1}{2}O_2(ads) + H_2O = X_2 + 2OH^-$$

Effect of CN^-. Pyrite is significantly depressed by KCN. In the absence of KCN pyrite recoveries of 100% are obtained at pH below 7, using 1×10^{-4} mol L^{-1} KEtX. Significant amounts of

pyrite are still present in the concentrate even up to pH 10. However, with a KCN addition of 6.0×10^{-3} mol L^{-1}, recovery is significantly depressed at pH 4 and completely depressed above pH 7.

Effect of pyrite depressants on copper recovery To assess the selective separation of copper ores from pyrite it is necessary to see how the copper floats under conditions identical to those reported for pyrite depression.

Chalcocite will float completely at up to pH 10 using 5.0×10^{-5} ethyl xanthate. The mechanism of flotation in the presence of amyl xanthate is similar to that of galena, with a chemisorbed cuprous amyl xanthate after which further xanthate additions form multilayers of cuprous xanthate in the compact layer, increasing the overall hydrophobicity.

At pHs between 8 and 10, the addition of sodium sulfide will depress pyrite without significantly altering the chalcocite recovery. The most effective depressant for this separation does however appear to be potassium cyanide which hardly affects the chalcocite recovery between pH 8 and 12 while virtually completely suppressing the pyrite over this range.

Chalcopyrite will float at 100% recovery over the pH range 2–12 both with 1×10^{-5} mol L^{-1} ethyl xanthate and 1.3×10^{-5} mol L^{-1} dixanthogen. No depression in recovery is observed up to pH 13. From this it may be inferred that at these high pHs it is the stability of the cuprous ethyl xanthate which effects flotation.

As chalcopyrite contains iron it is to be expected that it will to some extent be affected by the pyrite depressants but will be less sensitive to NaCN additions than the pyrite. For example, in a system where 60.9% pyrite recovery was achieved simultaneously with 90.5% chalcopyrite recovery with no depressant at pH 8.8, the addition of 0.04 kg ton^{-1} NaCN changed these figures to 26.1% pyrite recovery and 84.2% chalcopyrite recovery. Further additions of cyanide reduced the pyrite recovery to 15.6%, but also cut the chalcopyrite recovery to 31.0%.

Finally, it should be noted that sodium sulfide will depress chalcopyrite more than pyrite. This is due to the preferential formation of cupric sulfide over that of cuprous ethyl xanthate.

Flotation of oxides and silicates Oxides and silicates are the most abundant minerals in the earth's crust. Their flotation behaviour is important both because of their inherent value and because they act as gangue in the flotation of other minerals. Once again only a sample of the separations of interest can be discussed. Consider firstly the separation of quartz from haematite in iron ore processing.

Fuerstenau and Healy have suggested six possible procedures, four of which have been successfully employed in industry. These are based on the ζ-potential for haematite being positive in the pH range 2–4 with a PZC in the region of pH 6, while for quartz over the same range the ζ-potential is negative with a PZC at pH 2.

These procedures are:

- Flotation of haematite using an anionic sulfonate collector, for example sodium dodecyl benzene sulfonate which will adsorb on the positively charged haematite surface but not on the negatively charged quartz.
- Flotation of the haematite by the chemisorption of a fatty acid collector at pH 6–8. Chemisorption on the quartz will not occur because of its large negative ζ-potential at this pH.
- Reverse flotation of quartz at pH 6–7 using a cationic collector, for example, amylamine which will adsorb on the highly negatively charged quartz but not on the essentially uncharged haematite.
- Reverse flotation of quartz activated with calcium ions, with a long-chain fatty acid collector and the haematic depressed through the addition of starch. The hydrophilic starch molecules will chemisorb on the haematite through their carboxyl groups. Without the starch the haematite would also float under these conditions.

The successful implementation of these separations is clearly consistent with the electrostatic theory of collector adsorption.

Further thoughts on the electrostatic model of flotation. For collectors to function through physical interactions they must be present as counterions in the compact layer. Under these conditions the net charge on the outer boundary of the diffuse layer is reduced and hydrophobic interactions with the nonpolar surfactants on the bubble surface can occur. Iwasaki *et al.* reported very interesting results relating to the flotation of goethite (FeOOH). Goethite has a PZC at pH 6.7 and they measured flotation recoveries, in a laboratory Hallimond tube, as a function of pH using 1.0×10^{-3} mol L^{-1} of the anionic collectors sodium dodecyl sulfate and sodium dodecyl sulfonate and the cationic collector dodecyl ammonium chloride. They achieved effectively 100% recoveries up to pH 6.0 using the anionic collectors with the recovery falling effectively to zero above pH 7.0.

The recovery of goethite vs pH using the 1.0×10^{-3} mol L^{-1} cationic dodecylammonium chloride was the inverse of this with virtually no recovery up to pH 6.0 and 100% recovery between

pH 8 and 12.2 when the recovery fell to zero because the quaternary ammonium salt hydrolysed to the parent amine.

The increased flotation response at lower pHs with the anionic collectors is associated with an increased charge density σ_S in the compact layer which causes larger amounts of collector to be present as counterions. The increased concentration of their non-polar groups in the compact layer will increase the particle's hydrophobicity.

Modi and Fuerstenau reported tests on corundum (Al_2O_3), which has a PZC at pH 9, at four different pH values using an anionic collector, sodium dodecyl sulfate, at concentrations ranging between 10^{-7} and 10^{-1} mol L^{-1}.

At pH 4.0, 100% recovery was achieved with 0.5×10^{-4} mol L^{-1}, but it required 10 times that concentration for 100% recovery at pH 6.0, while at pH values of 9.3 and 11.0 the highest recovery achieved was only 30% at a reagent concentration of 10^{-3} mol L^{-1}.

Effect of the length of the hydrocarbon chain on the collector performance. Data have been reported for the flotation of quartz (PZC at pH 2.0) at pH 6–7, using the cationic alkylammonium acetates, with the alkyl chain length varying between C_4 and C_{18}. Incipient flotation occurs from about 10^{-8} mol L^{-1} for C_{18} to 10^{-1} for C_4. Similarly high rates are observed at 10^{-6} mol L^{-1} for C_{18} to 0.5 mol L^{-1} for the C_4. The onset of the high flotation rates are equated to the onset of hemimicelle formation.

Frothers

Chemical types A frother is a surface-active chemical whose principal function is to increase significantly the dispersion of air at a given aeration rate in the pulp phase of a flotation machine by producing small bubbles; this is done through the reduction of the surface tension at the air–water interface. If the pressure of the dispersed air is p_0 and the hydraulic pressure in the liquid at the aerator is p_b then the bubble radius R_b will be:

$$R_b \approx \frac{2\gamma}{(p_0 - p_b)} \qquad [41]$$

Laskowski has reviewed the mechanism of the action of surface-active reagents in flotation. He said that frother molecules have an uneven distribution of polar and non-polar groups which cause them preferentially to orientate at the air–water interface with the polar groups forming a liquid film around the bubble by hydrogen bonding with the water and the non-polar groups forming a gaseous film within the bubble. They may be classified into five groups:

1. Aliphatic alcohols with a single hydroxy group R–OH, where R is either a straight-chain alkyl group with five to eight carbon atoms or a branched chain with six to sixteen carbon atoms. Typical of the branched alcohols are methyl iso-butyl carbinol (MIBC), di-acetone alcohol and 2-ethyl hexanol. These frothers produce fine-textured, fairly selective froths.
2. Cyclic alcohols. These are represented by pine and eucalyptus oils of which the active components are the terpene alcohols typically α-terpineol. These are traditional frothers and are still used usually in combination with other frothers and collectors in 30% of the world's copper concentrators.
3. Phenols of which cresylic acid a mixture of cresols and xylenols, is the most commonly used.
4. Alkoxyparaffins of which the most successful is 1,1,3-triethoxybutane, have come into use in sulfide flotation as they seem also to have collector specificity.
5. Finally the polyglycols, particularly polypropylene glycol, these are available as commercial products with the general formula $R(X)_nOH$, where R is either H or C_nH_{2n+1} and X is either ethylene oxide (EO) $-CH_2CH_2O-$, propylene oxide (PO) $-CH_2CH(CH_3)-O-$ or butylene oxide (BO) $-CH_2CH_2CH(CH_3)-O-$. In the PO and BO frothers the propylene and butylene groups are hydrophobic and the ether oxygen and the hydroxyls are hydrophilic. Varying the relative length of the hydrophobic to hydrophilic groups in the molecule permits tailoring the molecule to a specific application.

Bubble stability in pulp The crucial property of a bubble in an aerated flotation cell relates to its ability to survive the collision and attachment of a particle without bursting. Although it is possible to observe that the addition of frothers does increase the stability of a single bubble, a coherent quantitative stability model does not exist. This will need to relate to the ability of its water film surrounding the bubble to withstand local disturbances. This ability is thought to be related to dynamic changes in surface tensions in the film following the local decreases in frother concentration after distortion has occurred following impact with a particle.

The effect of frother concentration on the surface energy of the solution has been used by Laskowski to characterize the surface activity of various frothers as related to their molecular structure. This is based on the application of the Gibbs adsorption isotherm, where Γ is the surface excess of the surface-active

agent, a its activity in the bulk solution and γ_{LV} is the bubble–liquid interface energy:

$$\Gamma = -\frac{a}{RT} \times \frac{\partial \gamma_{LV}}{\partial a} \qquad [42]$$

This implies that a decrease in a, the surfactant activity, at the gas–liquid interface following local surface increases, will be associated with a very sensitive surface tension γ increase.

Bubble–Particle Collision Dynamics

Interception efficiency – single bubble – particle collision Flint and Howarth observed that for a rational basis for flotation cell design to be achieved it is necessary that methods for the prediction of bubble–particle collision and subsequent adhesion be available.

For a single particle falling under gravity in the path of a single rising bubble, they provided a general definition of collision efficiency E, as the ratio of the number of particles which collide with the bubble to the number that would have collided if the liquid streamlines had not been diverted by the bubble. Their analysis is based on calculating the trajectories of single particles, initially remote from the bubble, and which are a distance δ from the centreline of the path of the rising bubble (**Figure 6**). Although all the liquid will pass around the bubble, particles on streamlines which pass closer to the bubble than the radius of the particle, are deemed to have come into contact with the bubble.

Calculation of single particle trajectories The bubble and particle are both assumed to be spherical, with the bubble of radius R_b rising vertically at a velocity U, and the particle of radius R_p falling under gravity. The trajectory calculation begins at a point where the lateral components of the flow field ahead of the rising bubble begin to induce a sideways motion of the particle. At this point the particle is considered to be offset by a distance, δ, from the centreline of the rising bubble.

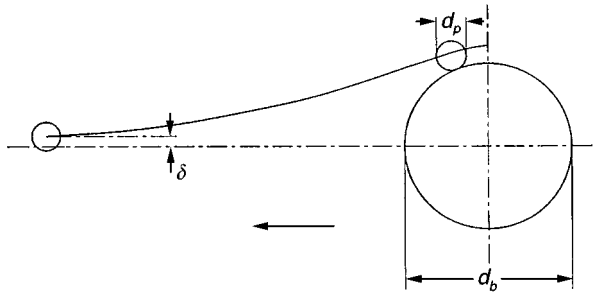

Figure 6 Single particle trajectory in the region of a rising bubble. Reproduced with permission from Flint and Howarth (1971) The collision efficiency of small particles with spherical air bubbles. *Chemical Engineering Science* 26, 1155–1168.

The consequence of the flow field assumed by the authors is that the trajectory is defined by the initial δ. A grazing trajectory is defined where for particles with an initial offset δ_0, the trajectory passes at a distance R_p from the bubble shell on its horizontal diameter. For particles at smaller offsets, contact will be made at some point on the bubble shell, while those with $\delta > \delta_0$ will make no contact.

The collision efficiency then follows:

$$E = \frac{\delta_0^2}{(R_b + R_p)^2} \qquad [43]$$

The particle trajectories under the influence of gravity and the flow pattern ahead of the rising bubble can be computed by integrating eqn [44] with the initial offset δ as a boundary condition. The liquid flow field ahead of the rising bubble is described in two dimensions, y (vertical) and x (horizontal), by its local velocity components u_y and u_x (assuming axisymmetric flow) using either the Stokes' or the potential flow stream functions. As the particles are very small ($R_p < 100$ μm) consideration of the interaction between the flow fields of particle and fluid is not necessary. The motion of the particle is described by its velocity components v_y and v_x.

The velocity components are normalized by dividing by U and setting the dimensionless time $t^* = tU/R_b$. The equations can then be expressed in terms of the dimensionless parameters K and G, where $K = (2\rho_P R_p^2 U)/(9\mu_F R_b)$ which is directly related to the ratio of inertial to drag forces on the particle while $G = (2[\rho_P - \rho_F]R_p^2 g)/(9\mu_F U)$ represents the terminal settling velocity of the particle in an undisturbed fluid:

$$K\frac{\partial v_x^*}{\partial t^*} = u_x^* - v_x^*$$
$$K\frac{\partial v_y^*}{\partial t^*} = -G - u_y^* + v_y^* \qquad [44]$$

Although this treatment greatly oversimplifies the flow processes in a highly aerated well-stirred suspension of particles in water, it does make interesting statements about the effects of bubble size on the efficiency of collection of a single particle of a given size and density.

Flint and Howarth report the fractional collision efficiency, E, as a function of the parameters K and G. For K values less than $0.1E$ is a function of G only

according to:

$$E = \frac{G}{G+1} \qquad [45]$$

The upper limit of $K = 0.1$ corresponds for example to a situation of 20 μm particles in an aerated suspension of 0.2 mm bubbles. Bubbles of this size will rise through still water at $U = 5\ \text{cm s}^{-1}$.K for silica, chalcopyrite and galena under these conditions is respectively 0.06, 0.095 and 0.17; the corresponding G values are 0.028, 0.055 and 0.11.

Using eqn [45], the respective collision efficiencies are 0.027, 0.052 and 0.10. If the bubbles in the aerated suspension were larger, the collision efficiencies would drop. For example for 0.4 mm bubbles whose rise velocity $U = 10\ \text{cm s}^{-1}$, the K values would fall further below 0.1 and the G values would also fall to 0.014, 0.027 and 0.055 with corresponding E values of 0.014, 0.026 and 0.052.

Thus, while 0.4 mm bubbles are probably satisfactory for floating chalcopyrite and galena, it might be necessary to generate smaller bubbles to float silica selectively. However, 60 μm silica particles will be efficiently floated with 1 mm bubbles. The bubble size required for the effective flotation of 60 μm chalcopyrite and galena need be no smaller that 5 mm.

These observations are obviously of both technical and economic importance, as while it is unnecessary to generate small bubbles for medium-size sulfide mineral particles, for light silicate mineral particles it may be necessary for selective separation to aerate the pulp suspension down to 100 μm microbubbles.

Bubble–particle contact time – general Following initial interception of the particle by the bubble, two possible modes of contact have been proposed.

First, the bubble shell is considered to deform elastically and for the particle either to attach to the bubble, or ultimately to be expelled from the shell under the elastic forces. The contact time is that lapsing between the moment of initial contact when the surface begins to deform, to the time when it first regains its original undistorted shape, subsequent oscillations being ignored.

In the second technique the particle after collision with the bubble is assumed to remain in contact with an undeformed surface, while being swept around from the point where it initially made contact, until it approaches the bubble's wake, where it is detached from the shell. The contact time according to this method is the time lapsed between the original contact to that when it first enters the bubble's wake.

Contact time assuming bubble – shell deformation Ye and Miller developed a model based on estimating the penetration distance $h(t)$ of a particle into the bubble shell. **Figure 7** shows their concept of defining $h(t)$ for the special case when contact is made on the line of centres. The deformed area increase is approximated in terms of $h(t)$ as:

$$A(t) = \pi h(t)^2 \qquad [46]$$

The force resisting the motion of the particle after collision is described in terms of the increase in the surface free energy of the deforming bubble surface:

$$dG_A = \gamma dA(t) = 2\pi\gamma h(t) dh(t) \text{ and the resisting force}$$

$$F(t) = \frac{dG_A}{dh(t)} = 2\pi\gamma h(t) \qquad [47]$$

The particle and the bubble approach each other at a relative velocity v^*. The position of the initial point of contact by the particle at the bubble surface is defined by an angle α between the contact point and the bubble centre and the centreline of the rising bubble.

The deformation is presumed to occur along the radial angle α at a relative velocity v_b^*. After impact the motion of the particle is resisted by the deforming bubble surface and is decelerated to zero. It is then accelerated in the reverse direction by the shell tension until it reaches the local bubble velocity, at which time it is presumed to lose contact with the

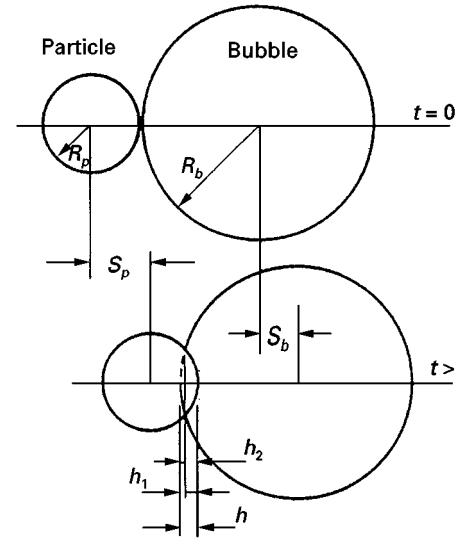

Figure 7 Bubble–particle contact time. Reproduced with permission from Ye and Miller (1988) Bubble/particle contact time in the analysis of coal flotation. *Coal Preparation* 5, 147–166.

bubble. If, however, the water film between the particle and the bubble during the deformation is thinned to the point of rupture then attachment will follow.

By assuming an average touching angle of $\sin^{-1}(2/3)$ they quote, for the overall contact time τ in seconds:

$$\tau = 13.5 \times \sqrt{\left(\frac{\pi \bar{m}_b m_p}{\gamma(\bar{m}_b + m_p)}\right)} \qquad [48]$$

Figure 8 shows contact times calculated using eqn [48] for a particle with a specific gravity of 2.6. It can be seen that if the particle mass is very much greater than the effective bubble mass then the contact time depends only on the bubble size.

Contact time assuming sliding contact Dobby and Finch have developed a model to predict contact time following an initial particle–bubble shell contact, at an angle α_n with respect to the centre of the bubble. The particle is pressed against the shell surface by its settling velocity $v_T \cos\alpha$ in the inward direction to the bubble centre while it is also being driven tangentially by the liquid moving in close contact with the bubble shell, at a velocity u_α. It leaves the shell at an angle α_m at which point its inward radial motion is equal the outward radial component of the surface liquid. The particle contact time t_s follows from the length of the arc between α_n and α_m divided by its tangential velocity $v_{p,\alpha}$:

$$\mathrm{t_s} = \int_{\alpha_n}^{\alpha_m} \frac{\pi(d_b + d_p)}{v_{p,\alpha}} \, \mathrm{d}\alpha \qquad [49]$$

This gives a sliding contact time in terms of an average $v_{p,\alpha}$ which is computed using an average vorticity $\xi_{s,\mathrm{avr}}$ and an average value for $\sin\alpha$, with α in degrees:

$$t_s = \frac{(\alpha_m - \alpha_n)}{360} \times \frac{\pi(d_b + d_p)}{\bar{v}_{p,\alpha}} \qquad [50]$$

Figure 9 shows sliding times computed for a 160 μm particle, of density $\rho_p = 2.5\ \mathrm{g\ cm^{-3}}$ with a terminal settling velocity $v_T = 1.58\ \mathrm{cm\ s^{-1}}$, on 3 mm bubbles rising at $v_b = 8.42\ \mathrm{cm\ s^{-1}}$ giving an approach velocity of $10\ \mathrm{cm\ s^{-1}}$. These times show a linear dependency on the angle of contact decreasing from 40 ms at $\alpha_n = 20^\circ$ to 0 when $\alpha_n = \alpha_m = 90^\circ$.

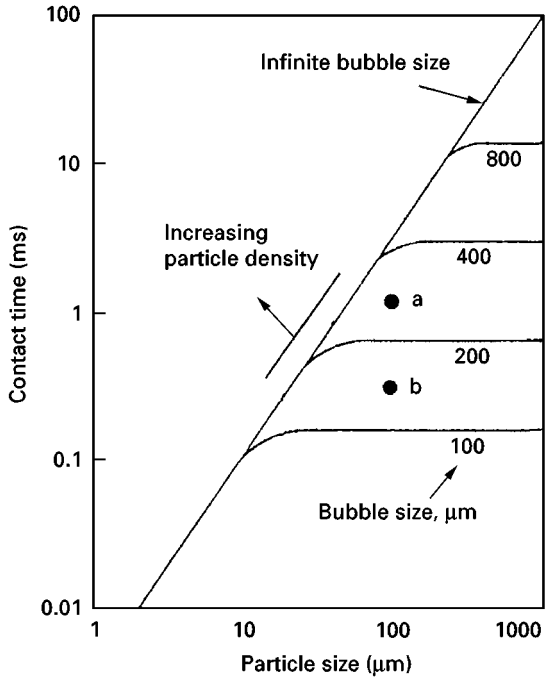

Figure 8 Particle bubble contact times. Reproduced with permission from Ye and Miller (1989) The significance of bubble/particle contact time in the analysis of coal flotation. *International Journal of Mineral Processing* 25, 199–219.

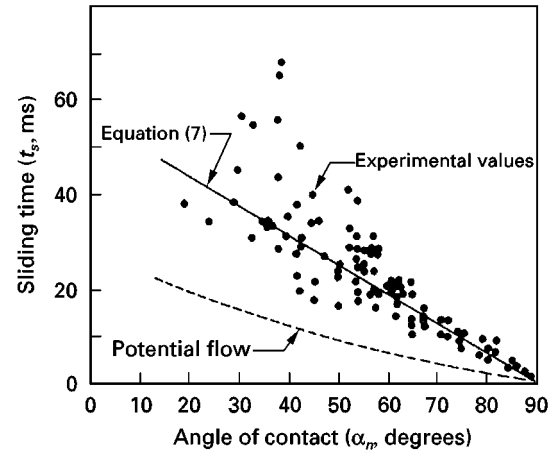

Figure 9 Particle bubble sliding contact times. Reproduced with permission from Dobby and Finch (1985) A model for particle sliding time for flotation size bubbles. *Journal of Colloid and Interface Science* 109(2), 493–498.

Thinning of the Water Film Attachment

Induction time–critical thickness Li, Fitzpatrick and Slattery have developed a mathematical model from which the attachment between the bubble and the particle can be characterized. The model relates to an initially spherical bubble approaching a stationary spherical particle. As the bubble–particle separation reduces, the water film separating them will thin and possibly reach a *critical thickness* at which it will rupture.

The *induction time* is the time between the initial contact, defined by the formation of a dimple on the bubble surface, and the final rupture of the separating film. Restating the previous sentence, a condition for attachment is for the *induction time* to be shorter than the *contact time*.

The model is defined in axisymmetric cylindrical coordinates with the z-axis coinciding with the line of approach of the bubble and particle centres. The particle is assumed to be spherical of radius R_p and the bubble away from the neighbourhood of close approach is also to be assumed spherical with a radius R_b. The origin of the system is taken as the centre of the spherical particle, the frame of reference being stationary with reference to the particle.

Figure 10 shows the bubble–film interface $z = h_1(r, t)$ and the surface of the solid $z = h_2(r)$. The surface of the bubble is dimpled on the nearest point of approach to the particle on the line of centres, the rim of the dimple is located at a radius $R(t)$ from the line of centres.

It has been assumed that the initial time of the bubble–particle contact $t = 0$ occurs when the thinning rate in the film becomes dependent on radial position.

The film thickness between the two surfaces $h_x(r, t)$ is given by the difference:

$$h_x(r, t) = h_1(r, t) - h_2(r)$$
$$h_0 = h_x(r, 0) \quad \text{and} \quad R_0 = R(0) \qquad [51]$$

For the spherical solid particle:

$$h_2(r) = (R_p^2 - r^2)^{1/2} \qquad [52]$$

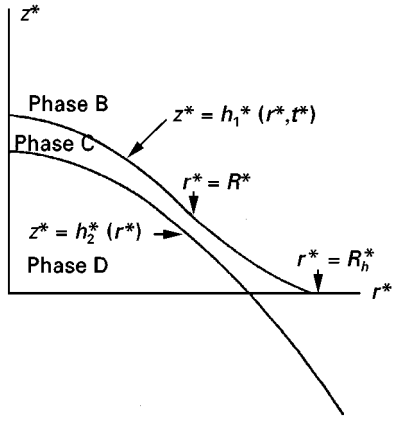

Figure 10 Thin liquid film formed as a small bubble approaches a small solid particle. Reproduced with permission from Li, Fitzpatrick and Slattery (1990) Rate of collection of particles by flotation. *Industrial Engineering Chemistry Research* 29, 955–957.

The thinning of the film is due to the pressure in the film $P(r, t)$ being greater than the hydraulic pressure p_h remote from the line of centres; at this point $r = R_h$. The pressure inside the bubble p_0 is linked to the hydraulic pressure p_h by:

$$p_h = p_0 - 2\frac{\gamma}{R_b} \qquad [53]$$

Components of the thinning pressure in the film

The local total film pressure $P(r, t)$ has three components: (a) the London–van der Waals interactive pressure π_v, (b) the electrostatic π_{el} pressure due to the charges on the solid and the bubble surfaces, and (c) a pressure π_{cap} caused by the deformation of the bubble surface from that of a sphere to $z = h_1(r, t)$, in the neighbourhood of the solid particle.

For the van der Waals component, π_v, for a film of thickness h_x the following is considered:

$$\pi_v = \frac{B}{h_x^m} \qquad [54]$$

When the film thickness was greater than 400 Å, $m = 4$ and $B = 10^{-19}$ erg cm, but when the film thickness was less than 120 Å the corresponding values were taken as $m = 3$ and $B = 10^{-14}$ erg.

These values are consistent with those quoted earlier for the Hamaker constant A. When B is positive the London–van der Waals forces between liquid–gas and the solid–liquid interfaces are mutually attractive.

The electrostatic interaction potential π_{el} between the particle–water and the water–bubble surfaces is given by:

$$\pi_{el} = \Delta \exp(-\kappa h_x) \qquad [55]$$

where:

$$\kappa^2 = \frac{8\pi n z_i^2 e^2}{DkT}$$

$$\Delta = 64nkT \tanh\left[\frac{z_i e \psi_{s\text{-}w}}{4kT}\right] \tanh\left[\frac{z_i e \psi_{w\text{-}g}}{4kT}\right]$$

where $\psi_{s\text{-}w}$ and $\psi_{w\text{-}g}$ are the electrostatic potentials at the bounding interfaces. When the interfaces have the same sign, Δ is positive and the surfaces are mutually repulsive and when the signs are different, Δ is negative and the surfaces are mutually attractive.

As deformation of the bubble surface occurs, the capillary pressure in the film $\pi_{cap}(r, t)$ is a function of

the mean curvature H_1 and the bubble pressure:

$$\pi_{cap}(r, t) = p_0 - 2H_1\gamma \qquad [56]$$

where γ is the surface tension of the distorted film:

$$\pi_{cap}(r, t) = p_0 - \frac{\gamma}{r}\frac{\partial}{\partial r} r \frac{\partial z_1(r, t)}{\partial r}$$

A lateral pressure gradient will develop in the water film normal to the separation distance h_x. Under this pressure gradient water will move to the bulk liquid, causing thinning:

$$\frac{\partial P(r, t)}{\partial r} = \frac{\partial}{\partial r}\left(\frac{B}{h^m} - \Delta e^{-\kappa h} - 2\gamma H_1\right) \qquad [57]$$

assuming that the van der Waals and the electrostatic disjoining pressures are attractive. To calculate the induction time it is necessary to obtain values for the velocity components of the water in the flowing film $v_r(r, z, t)$ and $v_z(r, z, t)$ in terms of the pressure gradient. For an incompressible Newtonian fluid with constant viscosity, the momentum balance equation for creeping flow for radial symmetry $v_\theta = 0$ and for negligible pressure variation in the z-direction reduces to:

$$\frac{\partial P}{\partial r} = \mu \frac{\partial^2 v_r}{\partial z^2} \qquad [58]$$

A solution for $v_r(z, r)$ at time t is obtained for both a mobile and an immobile bubble–water interface:

$$v_r(r, z) = \frac{1}{\mu}\frac{\partial P}{\partial r}\left[\frac{(z - h_2)^2}{2} - \frac{h}{n}(z - h_2)\right] \qquad [59]$$

where $n = 1$ for a mobile interface and $n = 2$ for an immobile interface. This, when substituted into the equation of continuity gives v_z, which together with v_r, gives a solution for the configuration of the bubble–water interface $z = h_1(r, t)t$. From this the change in film thickness at radial position r, with time follows:

$$\frac{\partial h_x}{\partial t} = \frac{1}{\mu}\frac{3 - n}{2n}\left[\frac{1}{3}h_x^3\left(\frac{\partial^2 P}{\partial r^2} + \frac{1}{r}\frac{\partial P}{\partial r}\right) + h_x^2\frac{\partial h_x}{\partial r}\frac{\partial P}{\partial r}\right] \qquad [60]$$

A radial position R_b is estimated, as the smallest value of R where the local bubble curvature is the same as that of the undeformed bubble. The force acting on the water film at the particles surface is then computed to be:

$$F(t) = 2\pi\int_0^{R_b(t)} (P(r, t) - p_0)\, dr \qquad [61]$$

The induction time is that when $F(t_{ind})$ is deemed just to have exceeded the adhesion energy of the solid–water interface. For the case where the effects of the electrostatic double layer can be neglected, the numerical integration shows an inverse power dependence of the induction time on the van der Waals parameter.

These conclusions have been tested against the experimental data reported by Ye and Miller whose observations were based on forcing a bubble through a solution on to a bed of particles for a predetermined time and recording as the induction time the time at which 50% of the events resulted in attachment.

The theoretical treatment predicts that when the particle radius R_p is very much smaller than the bubble radius R_b, $\log t_{ind}$ will be a linear function of $\log R_p$. This is consistent with the experimental data of Ye and Miller, although the predicted slopes are slightly lower than those reported.

When the electrostatic effects are allowed for the predictions have to be graphical as a general equation cannot be derived; there are also no experimental data available for checking. From **Figure 11** and **Table 3** it is, however, clear that these electrostatic effects are very significant.

Li, Fitzpatrick and Slattery have reported values for Δ and κ reproduced here as Table 3 which they used in conjunction with their derived relationships.

The data in the table are given for univalent ions and the surface potentials are given as equal on each surface, but both cases can be easily adapted. When the sign of the surface charges are opposite and the surfaces are consequently mutually attractive, Δ is negative.

The authors report induction times for a system corresponding to that of Ye and Miller although no direct comparisons with experimental data could be made. Figure 11 is typical of the predictions made.

For electrostatic interactive forces on a 100 μm particle in a 10^{-3} molar solution the induction times vary from 10 ms for $\pi_{el} = -80$ mV to more than a second for $\pi_{el} > +20$ mV.

As the solution molarity falls to 10^{-4} mV the induction time for $\pi_{el} = -80$ mV remains at 10 ms but falls to 100 ms for $\pi_{el} = +20$ mV.

The effect of particle size is also interesting; for a 10^{-3} molar solution and $\pi_{el} = -80$ mV the induction time is less than 1 ms for a 10 μm particle rising

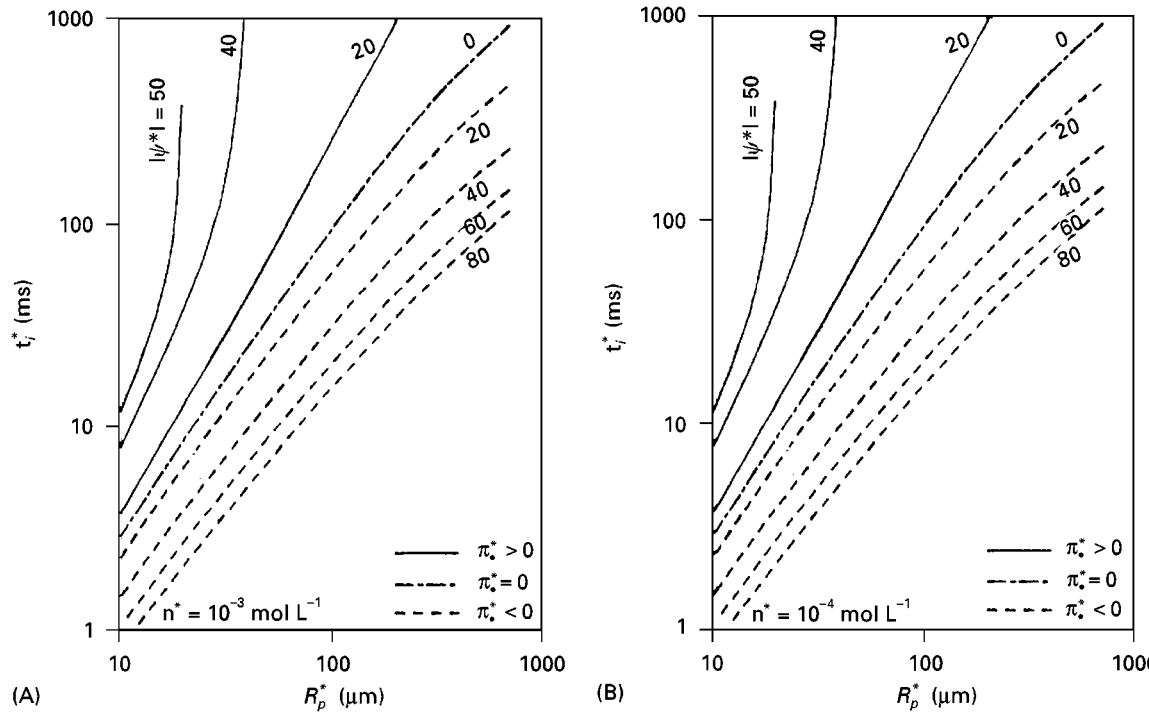

Figure 11 Induction times as a function of the charge density on particle and bubble surfaces, which are assumed equal but of similar or opposite signs, and the particle radius. (A) $n = 10^{-3}$ and (B) $n = 10^{-4}$ mol L^{-1}. Reproduced with permission from Li, Fitzpatrick and Slattery (1990) Rate of collection of particles by flotation. *Industrial Engineering Chemistry Research* 29, 955–957.

to 100 ms for a 1000 μm particle. The effect of a reduction in solution molarity to 10^{-4} does not, however, change the induction times significantly as it does in the previous case.

Although the model refers only to single bubble–single particle contact and the experimental data are similarly idealized, it is nevertheless valuable as it predicts induction times in fundamental terms which surely provides a sound basis for the experimental use of them as a characterizing parameter, for the development of reagent addition strategies for industrial separations.

Table 3 Showing values of Δ and κ as functions of surface potentials ψ_s, ψ_l at various solution molarities: 10^{-6}, 10^{-4}, 10^{-2} for univalent ions $z = 1$

$\pm\psi_S$ (mV)	$\pm\psi_L$ (mV)	$\pm\Delta$ at M (mols/litre)		
		10^{-6} (molar)	10^{-4} (molar)	10^{-2} (molar)
20	20	58.6	5.86×10^3	5.86×10^5
40	40	217.9	2.179×10^4	2.179×10^6
50	50	323.3	3.233×10^4	3.233×10^6
60	60	437.9	4.379×10^4	4.379×10^6
80	80	673.8	6.738×10^4	6.738×10^6
100	100	892.2	8.922×10^4	8.922×10^4
κ (cm^{-1})		3.257×10^4	3.257×10^5	3.257×10^6

Reproduced with permission from Li D, Fitzpatrick JA, Slattery JC (1990) Rate of collection of particles by flotation. *Industrial Engineering Chemistry Research* 29, 962, Table II.

Transfer across the Pulp–Froth Interface

The bubble structure at the top of the pulp is shown for two-phase foams in **Figure 12**. It can be shown that the rate at which bubbles are required to cross through a volume at the top of the pulp, described by the surface area of the cell multiplied by one bubble diameter, is determined by the overall aeration rate to the cell and the bubble size produced by the agitator or sparger.

The free rise velocity of a single bubble of a typical size produced in this way has a residence time significantly smaller than that calculated by dividing the liquid volume in the cell by the aeration rate. The dispersed bubble hold-up in the pulp is thus considerably less than that the bubble hold-up in the close-packed foam structure, producing a sharp discontinuity in the bubble volumetric fraction at the pulp–froth interface.

If, at the bottom of the foam layer the bubbles remain spherical in a closest-packed rhombohedral

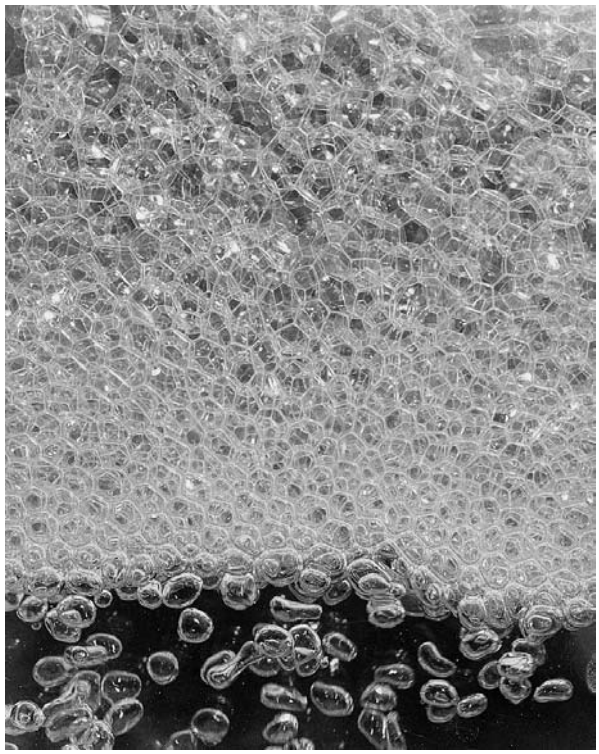

Figure 12 The structure of the interface between bubbles dispersed in water containing surfactant and the froth. No particles are present in this system.

structure, the volume fraction occupied by inter-bubble water will be $\varepsilon = 0.26$.

This means that solids transfer from the pulp to the froth in two ways. In the first the valuable particles are selectively attached to the bubble surface, while in the second the particles will be non-selectively entrained in the inter-bubble water. This entrainment will adversely affect the selectivity of the separation, but will apparently improve the total particle recovery.

Froth Microprocesses

Grade Enhancing – General

For the froth to perform a grade-enhancing (cleaning) function it is clearly necessary to reduce the entrainment of undesired solids.

The froth which forms at the pulp–froth interface is a close-packed structure of spherical bubbles (*kugelschaum*), which it will have a volumetric water fraction of about 30%. The solids content of this water will not have been selectively separated. To reduce the amount of entrained solids at the froth overflow it is necessary either to reduce the water content by drainage or to displace the solids in the inter-bubble water by adding external wash water at the upper froth surface.

Removal of Entrained Solids

Coalescence Froths with high water contents are mobile and overflow at high rates giving good recoveries at the expense of low grades. These froths occur when the bubbles on their upward passage from the pulp–froth interface through the froth to the overflow, retain their shape and do not coalesce.

It is theoretically possible that selective drainage of solids within the entrained water may occur, giving some grade improvements without a reduction in water content. However, the settling path within the froth is down the plateau borders and even with heavy minerals and low-density gangue, the differential settling rates are usually small and significant upgrading from this effect is uncommon.

The volume fraction of water in the *kugelschaum* can be reduced by allowing the close-packed spherical bubbles to coalesce to form a polyhedral structure (*polyederschaum*). The lower water content of this structure is related to the thinness of the water lamellae separating the flat polygonal sides of the bubbles.

The point at which three bubbles meet is called a plateau border. Drainage occurs down a network of these borders. At the plateau border the curvature of the bubble surfaces is relatively high. The difference between the curvature of the bubble surfaces at the plateau border and that of the flat sides, generates a capillary pressure which causes the lamellar water to flow towards the plateau border. This causes them to thin further to a point where they may rupture causing further coalescence.

The reduction of the froth water content by drainage is directly dependent on the degree of bubble coalescence which occurs during their passage upwards through the froth. This in turn depends on the stability of the inter-bubble lamellae of the *polyederschaum*.

The coalescence may possibly cause some rejection of the valuable solids into the draining inter-bubble water, and may also be associated with an increased bursting rate of the froth bubbles, which will also cause valuable solids to be rejected into the drainage water.

This suggests a linkage between the appearance of the overflowing froth and the cell performance. Regulation of the degree of coalescence which occurs in the froth is achieved by varying the addition of the frother. Woodburn, Austin and Stockton have reported experimental studies, carried out in a 1 litre laboratory Denver cell, relating to the removal of ash-forming mineral from a low-rank British coal. In these the demineralized coal is the valuable product and the ash-forming mineral the waste product. The tests relate on-line visual images to cell performance as characterized by grade-recovery curves

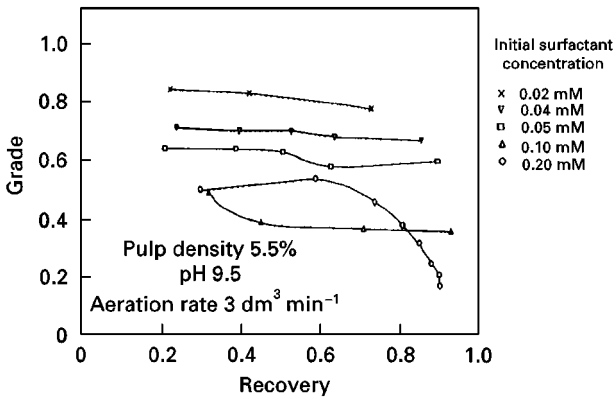

Figure 13 Grade recovery trajectories of batch coal flotation tests with varying initial single additions of the anionic collector/frother sodium dodecyl sulfate. Reproduced with permission from Woodburn ET, Austin LG and Stockton JB (1994) A froth based flotation kinetic model. *Chemical Engineering Research and Design* 72(A2), 211–226.

(**Figure 13**). There is a limiting achievable grade which reflects perfect separation. This is because, that even after fine grinding there is a residual inherent mineral content of the fine coal. This material which is determined in this case, by the ash content of the float fraction in a heavy medium (specific gravity of 1.4) centrifugal separation, is referred to as being unliberated.

Figure 13 shows a progressive reduction of grade with increasing recovery for a single test, and an overall grade reduction and recovery increase over all the tests, with increased addition of the frother/collector sodium dodecyl sulfate (SDS).

Each grade–recovery curve, with the partial exception of the run with 0.10 mM SDS initial addition, completely encloses all runs with higher initial additions. This run was done on a different coal sample from the same pit. **Tables 4–7** show that for the coal froths the average concentration of SDS in the concentrate increases as expected with increases in the initial dose, but does not change significantly over a run despite the observed increased coalescence.

In all the tests the concentrate was free-flowing and then terminated when the froth would no longer flow, and had a high bubble bursting rate. Both effects are consistent with lamellae thinning to below a thickness where lateral flow to the plateau border stops. The reduction of grade with time and increased coalescence, during the course of a single test, is however not consistent with the simple entrainment model.

A possible explanation for the grade reduction despite the increased coalescence, is that there may be a competitive adsorption of valuable and waste material on the bubble surface rather than perfect selectivity. As a batch test proceeds there is an increasing fraction of waste solids in the pulp, which may consequently cause a corresponding increase in the waste solid attachment to the bubble surface. The increasing waste solid concentration may also contribute to the decreased lamella stability, despite the presence of SDS, because of the lower repulsion between two closely adjacent bubble surfaces, rather than that between the two surfaces with a higher fraction of coal. These observations must be treated as speculative.

Figure 14 shows for the same series of tests the percentage of solids in the overflowing concentrates as a function of time. From this it can be seen that the water content of the concentrate increases with increased SDS addition. Comparison with the grade–recovery curves of Figure 13 clearly relates decreases in grade and increase in recovery with the concentrate water content. It is also interesting to note that the time of a single test increased with increased surfactant reflecting the increased stability of the bubbles in the froth. For the run with 0.2 mM initial SDS addition, the solids content in the overflowing froth towards the end of the run was about that of the pulp solids, which indicates almost complete entrainment.

Figures 15 and **16** show the appearance of the top surface of the froth for the runs with initial SDS additions of 0.04 and 0.05 mM L^{-1}, respectively.

Table 4 The effect of froth structures on flotation kinetics and selectivity

Time (s)	*Dry solids in sample (g)*	*Water in sample (g)*	*Ash (%w/w)*	*Mean bubble size (mm)*	*Sodium dodecyl sulfate concentration in water (μmolar)*	*Particle size d_{90} (μm)*
46.0	9.9	19.39	2.06	8.31	12.9	55.0
64.0	8.57	18.39	2.14	11.60	7.93	65.0
90.0	13.9	23.59	2.83	17.40	7.57	63.0
Tailings	12.77		37.6		0.64	45.0

Feed mass 49.5 g coal, feed ash 12.7%, total water 850.6 g, sodium dodecyl sulfate 0.02 mM. Reproduced with permission from Stockton J (1989) PhD thesis, UMIST, Manchester.

Table 5 The effect of froth structures on flotation kinetics and selectivity

Time (s)	*Dry solids in sample (g)*	*Water in sample (g)*	*Cum ash (%w/w)*	*Mean bubble size (mm)*	*Sodium dodecyl sulfate concentration in water (μmolar)*	*Particle size d_{90} (μm)*
7.0	10.93	51.37	3.64	3.07	24.06	67.0
30.0	7.11	37.19	3.78	4.29	23.7	60.0
47.0	5.92	23.98	3.81	5.12	38.6	63.0
62.0	4.63	15.62	4.10	4.67	45.0	62.0
105.0	10.23	14.07	4.23	–	68.4	70.0
Tailings	6.63	–	63.0	–	4.74	34.5

Feed mass 49.5 g coal, feed ash 12.7%, total water 850.6 g, sodium dodecyl sulfate 0.04 mM. Reproduced with permission from Stockton J (1989) PhD thesis, UMIST, Manchester.

Table 4 reports for the 0.04 mM run, an increase in the mean bubble size from 3.07 mm at 17 s to 4.67 mm at 62 s, while for the 0.05 mM run the mean bubble size varied from 1.7 mm at 23 s to 3.6 mm at 77 s.

The smaller bubbles of the 0.05 mM run corresponded with poorer grades and lower concentrate solids content than those observed in the 0.04 mM run. It can be seen that in both runs the mean bubble size as viewed from above increased with time of the test.

Figure 17 shows the junction of three bubbles after coalescence. The plateau border can be seen, as can be the plane liquid lamella separating two adjacent bubbles. The presence of solids on the bubble surfaces can also be seen. These show incomplete surface coverage.

Displacement washing The structure of a column flotation cell is quite different from that of the mechanical (sub-aeration) cells which have by implication formed the basis of this presentation. In both, air bubbles are dispersed through a suspension of solids in water, but while in mechanical cell this is done with an aerating agitator, in column cells air is dispersed from the bottom of the pulp through a sparger. In mechanical cells the aspect ratio is such that the cross-section is of the same order as the height of the cell while in column cells the depth of the collection/bubbling zone (pulp) is much greater than the cross-section. For instance Yianatos, Finch and Laplante quote for the molybdenum column cleaner and recleaner cells, at the Noranda Mínes, Gaspè in Quebec, cross-sections which are respectively 0.91 and 0.47 m square with overall heights of 12 m for both.

In the column cell the feed suspension is added near the top of the bubbling zone and the particles are free to settle. While they are settling they encounter the rising bubbles in a physical situation which is closer to that envisaged in the model of Flint and Howarth, than that in the strongly turbulent mechanical cells. The flow pattern of the rising gas bubbles and the settling solids approximates to plug flow whereas that in the mechanical cells is closer to perfectly mixed.

As with the subaeration/mechanical cells a froth phase forms above the aerated pulp/collection zone into which entrainment of water containing non-selectively separated solids occurs. In column cells, the inter-bubble water containing the unwanted

Table 6 The effect of froth structures on flotation kinetics and selectivity

Time (s)	*Dry solids in sample (g)*	*Water in sample (g)*	*Cum ash (%w/w)*	*Mean bubble size (mm)*	*Sodium dodecyl sulfate concentration in water (μmolar)*	*Particle size d_{90} (μm)*
23.0	9.7	56.9	4.62	1.7	36.9	64.0
39.0	8.11	43.1	4.55	2.4	31.2	64.0
57.0	5.17	27.7	4.67	3.2	37.7	66.0
77.0	5.69	24.7	5.28	3.6	53.8	63.0
180.0	12.09	14.2	5.07	10.00	122.7	54.0
Tailings	6.76	–	57.6	–	6.69	35.0

Feed mass 49.5 g coal, feed ash 12.7%, total water 850.6 g, sodium dodecyl sulfate 0.05 mM. Reproduced with permission from Stockton J (1989) PhD thesis, UMIST, Manchester.

Table 7 The effect of froth structures on flotation kinetics and selectivity

Time (s)	*Dry solids in sample (g)*	*Water in sample (g)*	*Ash (%w/w)*	*Mean bubble size (mm)*	*Sodium dodecyl sulfate concentration in water (μmolar)*	*Particle size d_{90} (μm)*
20.0	14.0	108.0	6.37	0.76	153.0	52.0
30.0	13.1	78.6	5.8	1.16	78.0	49.5
45.0	7.3	99.3	6.9	1.63	133.0	44.0
60.0	3.6	85.9	7.85	1.86	128.0	47.0
80.0	2.4	79.4	8.7	1.83	125.0	40.0
100.0	1.65	71.9	9.5	2.39	109.0	41.0
130.0	1.00	55.1	10.09	3.0	115.0	43.0
300.0	0.6	50.8	10.54	5.0	134.0	33.0
Tailings	1.4	–	68.82	–	51.0	34.5

Feed mass 49.5 g coal, feed ash 12.7%, total water 850.6 g, sodium dodecyl sulfate 0.02 mM. Reproduced with permission from Stockton J (1989) PhD thesis, UMIST, Manchester.

solids is displaced by spraying solids-free wash water on to the upper froth surface.

Yianatos, Finch and Laplante reported laboratory and plant studies relating to the effectiveness of the displacement washing. For the plant tests these involved a broad step pulse injection of 200–600 g of LiCl tracer dissolved in 5 L of water into the feedbox. The feedbox was 35 cm below the collection zone/froth interface. Tracer concentrations were measured 100 cm below the injection point, 10 cm into the froth above the interface, from the overflowing concentrate at the top of the froth and from the tailings stream at the base of the cell.

In the 0.91 m^2 cross-section cell, a froth zone varying between 45 and 130 cm depth was reported while in the 0.45m^2 cross-section cell the froth depth varied between 110 and 140 cm.

For all the runs reported virtually no tracer was detected in the overflowing concentrate, although at high superficial gas rates of 2 cm s^{-1} tracer was detected in the froth up to 70 cm above the interface. The tracer residence time distributions (RTD) after the pulse injection, at 35 cm below the froth interface, indicated significant mixing in the water between the

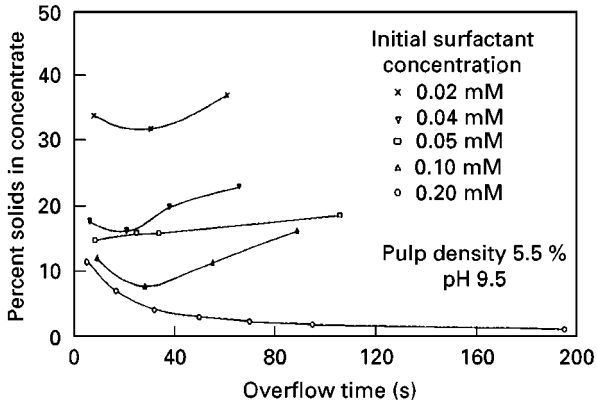

Figure 14 Percentage of coal solids in the overflowing concentrate at varying times during an individual test. The data are taken from the same tests reported in Figure 13. Reproduced with permission from Woodburn ET, Austin LG and Stockton JB (1994) A froth based flotation kinetic model. *Chemical Engineering Research and Design* 72(A2), 211–226.

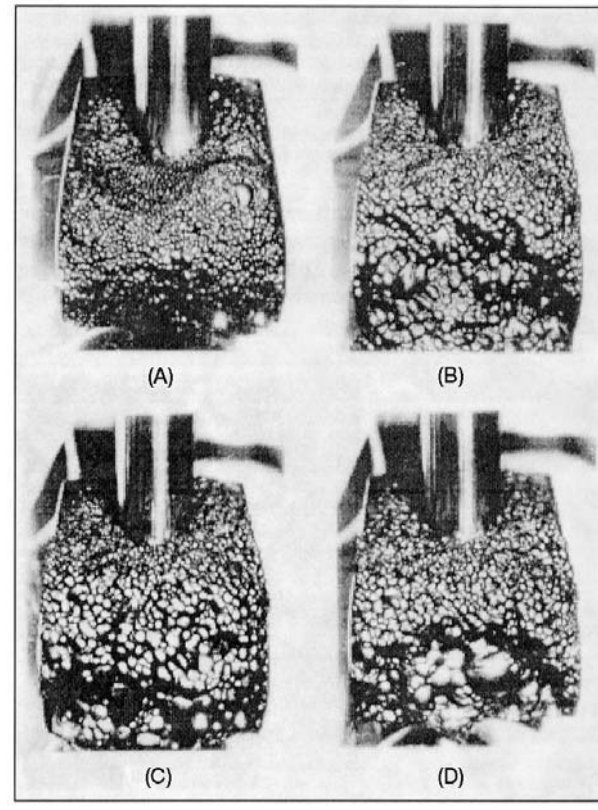

Figure 15 Photographs of overflowing coal concentrates. Single initial addition of 0.04 mmol L^{-1} sodium dedecyl sulfate: (A) after 24 s – first concentrate, (B) after 43 s – second concentrate, (C) after 55 s – third concentrate, (D) after 81 s – fourth concentrate. Reproduced with permission from Woodburn ET, Austin LG and Stockton JB (1994) A froth based flotation kinetic model. *Chemical Engineering Research and Design* 72(A2), 211–226.

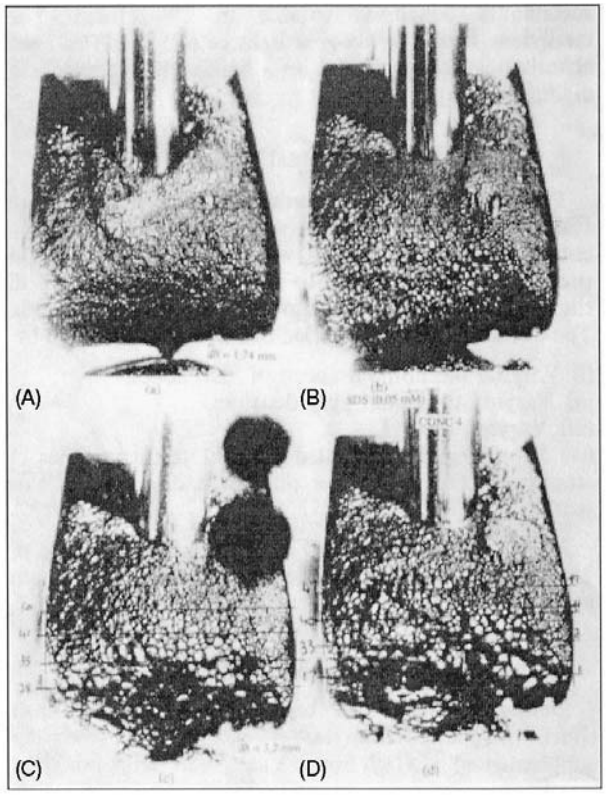

Figure 16 Photographs of overflowing coal concentrates. Single initial addition of 0.05 mmol L^{-1} sodium dedecyl sulfate: (A) after 31 s – first concentrate, average bubble diameter 1.74 mm; (B) after 50 s – second concentrate, average bubble diameter 2.35 mm; (C) after 66 s – third concentrate, average bubble diameter 3.2 mm; note 154 features identified on four lines; (D) after 92 s – fourth concentrate; note 137 features identified on four lines. Each line is 122 mm long. Reproduced with permission from Woodburn ET, Austin LG and Stockton JB (1994) A froth based flotation kinetic model. *Chemical Engineering Research and Design* 72(A2), 211–226.

feed point and the froth interface. Similarly, the tracer RTDs in the tailings stream showed significant axial mixing in the collection zone below the feed point.

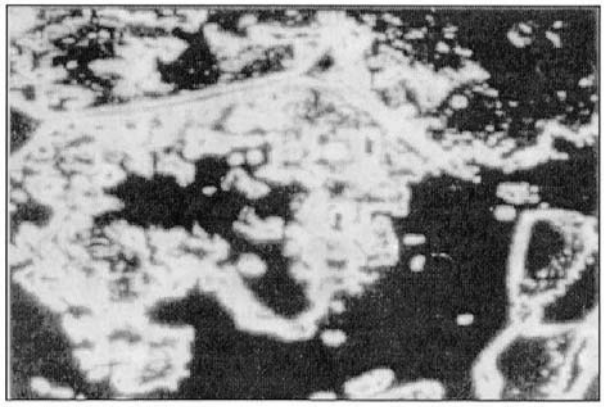

Figure 17 Image of the upper surface of coal-laden bubbles. Note the inter-bubble lamellae and plateau border.

For both cells the mean residence time of the tracer in the collection zone was approximately 10.0 min.

From these tests it seems that froth depths up to 100 cm may be needed to ensure complete removal of entrained solids from the final concentrate. These tracer studies are consistent with the high grades which are achieved in these cells.

There is a question relating to the capacity of column cells. The rate of flotation in both types of cell depends on the effectiveness of the bubble–particle collision and attachment processes. A key factor in the evaluation of these is the velocity of approach of the particle and the bubble. In the mechanical cells high approach velocities are achieved through the turbulence in the pulp. In column cells the approach velocity is determined by the bubble rise and particle settling velocities. For small particles, and hence small bubbles, these velocities are so low, that the collection zone must be impractically high if the necessary frequency of bubble–particle encounters is to be achieved. In industrial practice the column cells are most effective where high grades at low throughputs are required. This is particularly the case where previously produced concentrates have to be cleaned and re-cleaned.

Sam, Gomez and Finch have shown that the bubble rise velocity is reduced in the presence of surfactants over that in distilled water and further that the surfactant adsorption is a rate process. This retardation of the rising bubble appears to be a function of the surface immobility which in turn should improve attachment after a successful interception, by increasing the contact time with individual particles.

Tuteja, Spottiswood and Misra in reporting the reverse flotation of undesired talc from a gold-bearing pyrite ore, have shown that there is virtually no grade change with height in the collection zone but that there is a dramatic increase in the percentage of talc in the froth solids, increasing from 3% at the base of the froth to 50% at the concentrate overflow. At the same time the presence of an arsenic contaminant fell from 3750 ppm in the pulp solids to 750 ppm in the concentrate overflow.

Cell Design and Control

Outline of the Factors Influencing Single Cell Design

In general, the contractor is responsible for the engineering design of the cell, while the customer is responsible for the design of the separation system. This involves the selection of both chemical collectors, depressants and frothers and also the solution pH. The principles underlying these have been thoroughly discussed earlier.

In addition, the degree of pretreatment required to liberate the desired component from the waste, prior to the flotation separation, has to be decided. Obviously the two parties to the project have to interact and this is done in the first instance through laboratory and pilot plant trials, followed if possible by a large-scale plant trial.

The contractor's responsibility is to provide, within economic constraints, equipment in which dispersed bubbles of a specified size will be generated in the pulp, to achieve efficient bubble interception with particles of a specified density and size distribution. The fundamental considerations underlying this have been discussed earlier. There are two main types of equipment, which employ very different techniques for bubble–particle contact.

Mechanical sub-aeration cells In these cells the pulp is stirred vigorously by a centrally located agitator, on of whose functions is simply to prevent solids settling. In most cells the central agitator also induces air down an annulus surrounding its shaft and disperses the air radially as bubbles into the pulp. The intense turbulence generated by the agitator favours a high rate of bubble–particle collision, but also if the turbulent intensity is too high then previously attached particles may detach from the bubble surface.

The flow pattern in these cells divides into an intense inner region in the vicinity of the impeller, and a much larger less turbulent outer region in the bulk of the cell. In the relatively quiescent outer region the bubble–particle aggregates rise to form a froth. The cell design provides a sufficient depth between the pulp/froth interface and the overflow weir to permit drainage of some entrained solids. In commercial cells the froth can be removed by mechanical scrapers so froth mobility at the overflow is not usually a serious concern.

Finally, a class of cells should be mentioned in which specific attention is paid to achieving a high degree of bubble–particle contact without subsequent detachment. One example of this class of intensive cell, pumps the feed through a venturi nozzle which induces air under pressure into the low pressure region at the venturi throat. This causes bubbles to form which appear to nucleate on the solid particles.

Column cells In these cells particle–bubble interception occurs under low turbulent conditions essentially through particles settling under gravity meeting rising bubbles. The bubbles are introduced at the bottom of the collection zone through a sparger, and the feed particle suspension near the top of the collection zone. The low approach velocities of fine particles settling slowly and bubbles rising against down-flowing water reduce the interception rates, thus requiring more possible contacting opportunities, leading to very deep collection zones.

At the top of the collection zone a froth bed forms, which itself may be deep with bed depths of over 1 m being reported. The column cells produce very high purity products, achieved largely by the displacement of entrained water after adding wash water to the upper froth surface.

Multiple Cell Circuits

Circuit configuration In industrial operation it is necessary to have many cells in operation if the desired upgrading of large quantities of low-grade feed is required. The cells are operated in banks in which the tailings stream from one cell moves in sequence to the next. However, the concentrates are withdrawn from each individual cell into a concentrate launder which runs parallel to the cell bank.

Each bank then produces a single concentrate and a single tailings stream. These streams may in their turn be reprocessed. Typically, the first bank in a circuit would be called the rougher. The tailings stream from the rougher is then fed to the scavenger bank whose function is to recover any residual valuable material which may not have been floated in the rougher.

The concentrate stream from the rougher is fed to the cleaner bank whose function is to improve its grade. Finally, it may be necessary further to upgrade the cleaner concentrate by sending it to a recleaner bank. The circuit is completed by internal recycling. The final product of the circuit is the cleaner (recleaner) concentrate and the scavenger tailings.

The chemical environment of a particular bank of cells is determined by the addition of chemicals and pH regulators to the feedbox of the first cell of the bank.

Kinetic modelling For the design of circuits, a description of the kinetics of particle removal of any given cell to the concentrate overflow is required. Attempts to develop such a model have centred on the transfer rate in terms of the local concentration of a solid class in the pulp. This requires a matrix of deterministic single rate constants characterizing each solid species and particle size class within that species. These parameters can be determined either from batch cell tests or from the performance of a single continuously operating cell. Even with a large dimension matrix of rate constants, the ability of the model to predict accurately circuit performances of operating plant, is limited. The fundamental weakness of this approach is that it treats the pulp and the froth as

one, ignoring the very different subprocesses affecting separation in each of the phases.

On-line control The difficulty of implementing on-line control is the necessity for off-line analysis of solid grades and to a certain extent off-line measurements of the mass flow of solids and water at different points in the circuit.

Informal operational control is performed by experienced operators following subjective comparisons of the appearance of overflowing froths, with a desired structure. The advantage of this approach is that the structure of the overflowing froth is easily observable and corrective actions can be rapidly implemented.

Currently several groups of academic workers are working on quantifying the froth characterization using on-line image analysis, with promising results. This is, of course, only a first step in the development of a feedback control system by which optimum operation can be effected.

This is an exciting development which can be anticipated with some confidence to lead to implemental optimal control strategies.

See Colour Plates 10, 11.

Further Reading

Adamson AW (1982) *Physical Chemistry of Surfaces*, 4th edn. New York: John Wiley.

American Institute of Chemical Engineers (1975) *Natural and Induced Hydrophobicity in Sulfide Mineral Systems*. AIChE Symposium Series, Vol. 71, No. 150. New York: AIChE.

Fuerstenau DW (ed.) (1962) *Froth Flotation, 50th Anniversary Volume*. New York: American Institute of Mining Metallurgical and Petroleum Engineers.

Fuerstenau DW and Healey TW (1972) *Adsorptive Bubble Separation Techniques*, Chap. 6. New York: Academic Press.

Fuerstenau MC (ed.) (1976) *Flotation. AM Gaudin Memorial Volumes I and II*. New York: American Institute of Mining Metallurgical and Petroleum Engineers.

King RP (ed.) (1982) *Principles of Flotation*, Monograph Series No. 3. Fuerstenau MC. *The Flotation of Oxide and Silicate Minerals*; Fuerstenau MC and Fuerstenau DW. *Sulphide Mineral Flotation*; Lovell VM. *Industrial Flotation Reagents*: (a) *Structural Models of Sulphydryl Collectors*, (b) *Structural Models of Anionic Collectors*, (c) *Structural Models of Frothers*. Johannesburg: South African Institute of Mining and Metallurgy.

Klassen VI and Mokrousov VA (1963) *An Introduction to the Theory of Flotation*. London: Butterworths.

The Interface Symposium (1964) *Attractive Forces at Interfaces. Industrial and Engineering Chemistry* Vol. 56, No. 12.

Laskowski JS (1989) *Frothing in Flotation: A Volume in Honor of Jan Leja*. New York: Gordon & Breach.

Laskowski JS (1993) *Frothers and Flotation Froths. Mineral Processing and Extractive Metallurgy Review*, Vol. 12. New York: Gordon & Breach.

Laskowski JS and Woodburn ET (eds) (1998) *Frothing in Flotation II*. Amsterdam: Gordon & Breach.

Leja J (1982) *Surface Chemistry of Froth Flotation*. New York: Plenum Press.

Sebba F (1987) *Foams and Biliquid Foams – Aphrons*. New York: John Wiley.

ION EXCHANGE

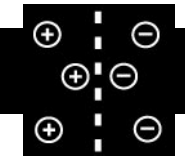

A. Dyer, University of Salford, Salford, UK

Introduction

Ion exchange has been described as the oldest scientific phenomenon known to humanity. This claim arises from descriptions that occur in the Bible and in the writings of Aristotle, but the first truly scientific allusion to ion exchange is attributed to two English agricultural chemists in 1850. These were J. T. Way and H. S. Thompson, who independently observed the replacement of calcium in soils by ammonium ions. This discovery was the precursor to the study of inorganic materials capable of 'base' exchange, and in 1858 C. H. Eichorn showed that natural zeolite minerals (chabazite and natrolite) could reversibly exchange cations. The importance of this property in water softening was recognized by H. Gans who, at the turn of the century, patented a series of synthetic amorphous aluminosilicates for this purpose. He called them 'permutites', and they were widely used to soften industrial and domestic water supplies until recent times, as well as being employed in nuclear waste treatment. Permutites had low ion exchange capacities and were both chemically and mechanically unstable.

This early work has generated some myths commonly stated in elementary texts, namely that zeolite minerals are responsible for the 'base' exchange in soils and that permutites are synthetic zeolites. The presence of clay minerals in soils accounts for the majority of their exchange capacity, and zeolites by definition must be crystalline. Both these topics will arise later in this article.